

## YOUNG STELLAR OBJECTS IN THE MASSIVE STAR-FORMING REGION W49

G. SARAL<sup>1,2</sup>, J. L. HORA<sup>1</sup>, S. E. WILLIS<sup>1</sup>, X. P. KOENIG<sup>3</sup>, R. A. GUTERMUTH<sup>4</sup>, A. T. SAYGAC<sup>5</sup>*Received 2015 March 25; accepted 2015 September 17; published 2015 October 23*

## ABSTRACT

We present the initial results of our investigation of the star-forming complex W49, one of the youngest and most luminous massive star-forming regions in our Galaxy. We used *Spitzer*/Infrared Array Camera (IRAC) data to investigate massive star formation with the primary objective of locating a representative set of protostars and the clusters of young stars that are forming around them. We present our source catalog with the mosaics from the IRAC data. In this study we used a combination of IRAC, MIPS, Two Micron All Sky Survey, and UKIRT Deep Infrared Sky Survey (UKIDSS) data to identify and classify the young stellar objects (YSOs). We identified 232 Class 0/I YSOs, 907 Class II YSOs, and 74 transition disk candidate objects using color–color and color–magnitude diagrams. In addition, to understand the evolution of star formation in W49, we analyzed the distribution of YSOs in the region to identify clusters using a minimal spanning tree method. The fraction of YSOs that belong to clusters with  $\geq 7$  members is found to be 52% for a cutoff distance of  $96''$ , and the ratio of Class II/I objects is 2.1. We compared the W49 region to the G305 and G333 star-forming regions and concluded that the W49 has the richest population, with seven subclusters of YSOs.

*Subject headings:* infrared: stars — stars: early-type — stars: formation — stars: pre-main sequence

## 1. INTRODUCTION

It is generally accepted that approximately 70–90% of stars form in groups and clusters embedded in collapsing molecular clouds (Lada & Lada 2003; Bressert et al. 2010). Observations of nearby star-forming regions have revealed how a low-mass star can form in an isolated environment. However, massive stars play a vital role in the star formation process in embedded clusters, yet their own formation and their effects on subsequent generations of star formation are not well understood. Massive stars form relatively quickly compared to low-mass stars and reach the main sequence still embedded in their natal clump. The short duration of this phase means that these objects are relatively rare and thus typically more distant, making them difficult to study. In addition, the embedded clusters hosting those massive stars are hidden inside their natal molecular cloud and can only be observed at infrared (IR) and millimeter wavelengths.

The launch of the *Spitzer Space Telescope* in 2004 (Werner et al. 2004) has had a big impact on our understanding of the star formation process. Many nearby star-forming regions (e.g. Taurus complex, M16, M17, NGC 6334) have been studied (Torres et al. 2009; Kuhn et al. 2013; Willis et al. 2013), and many methods have been suggested and used to classify the young stellar objects (YSOs) through their spectral indices (Lada 1987; Robitaille et al. 2006) or color–color diagrams (Gutermuth et al. 2008, 2009). The combination of *Spitzer*-Infrared Array Camera (IRAC) (Allen et al. 2004; Fazio et al. 2004; Gutermuth et al. 2008) and near-IR data has been a powerful tool to identify and classify YSOs.

We performed a detailed investigation of the W49 star-forming region, which is located within one of the most massive giant molecular clouds (GMCs) ( $M_{\text{gas}} \sim 10^6 M_{\odot}$ ; Simon et al. 2001) in the Galaxy and hosts many massive protostars and clusters of young stars that are forming around them. Since it is not possible to observe a single YSO at various stages of its evolution, we have to observe large numbers of YSOs to study the pre-main-sequence evolution statistically (Lada & Adams 1992; Allen et al. 2004; Gutermuth et al. 2009).

The W49 star-forming region was discovered as a radio continuum source by Westerhout (1958) and lies in the Galactic plane ( $l, b = 43.1, 0.0$ ). The W49 GMC extends over more than 100 pc, assuming a distance of 11.1 kpc (Zhang et al. 2013). Gálvan-Madrid et al. (2013) derived a total mass  $M_{\text{gas}} \sim 1.1 \times 10^6 M_{\odot}$  within a radius 60 pc and  $M_{\text{gas}} \sim 2 \times 10^5 M_{\odot}$  within 6 pc from multiscale observations of CO. They concluded that the mass reservoir of the molecular cloud is sufficient to form several massive star clusters, or a small system of smaller, but still bound, clusters.

The W49 complex consists of two main components; a thermal source (W49A), which is a star-forming region, and a nonthermal source (W49B), identified as a supernova remnant (Mezger et al. 1967). W49A is one of the most luminous star-forming regions in the Milky Way ( $L_{\text{bol}} = 10^{7.2} L_{\odot}$ ; Sievers et al. 1991), with hundreds of candidate OB stars (Dreher et al. 1984; Dickel & Goss 1990; De Pree et al. 2000; Alves & Homeier 2003), and consists of the star-forming regions W49 north (W49N/G043.16+0.01), W49 south (W49S), and W49 southwest (W49SW). W49N also hosts the most luminous water maser in the Galaxy, at a distance of  $d = 11.4 \pm 1.2$  kpc (Gwinn et al. 1992). Zhang et al. (2013) redetermined this distance as  $11.1^{+0.79}_{-0.69}$  kpc by studying the water masers named G043.16+0.01 and G048.60+0.02. W49A hosts a ring of a dozen O stars and 25–30 ultracompact H II (UCHII) regions (Dreher et al. 1984; Welch et al. 1987; Dickel & Goss 1990; De Pree et al. 1997), which may represent a massive star cluster. Its mass has been estimated at  $M_{\text{cl}} \gtrsim 4 \times 10^4 M_{\odot}$  (Homeier & Alves 2005). Recently, Wu et al.

<sup>1</sup> Harvard-Smithsonian Center for Astrophysics, 60 Garden Street, Cambridge, MA 02138, USA

<sup>2</sup> Istanbul University, Graduate School of Science and Engineering, Bozdogan Kemerli Cad. 8, Vezneciler-Istanbul-Turkey

<sup>3</sup> Yale University, Department of Astronomy, 208101, New Haven, CT 06520-8101, USA

<sup>4</sup> University of Massachusetts, Department of Astronomy, Amherst, MA 01003, USA

<sup>5</sup> Istanbul University, Faculty of Science, Astronomy and Space Sciences Department, Istanbul-Turkey

(2014) discovered a very massive O2-3.5 spectral type star in the central cluster of W49A.

Several authors have tried to explain the nature of the star formation in W49A. Welch et al. (1987) postulated a large-scale gravitational collapse toward the central ring of hypercompact (HC) H II regions (Welch ring) in W49N, based on their observations of molecular lines that exhibit a double-peaked profile. On the other hand, Serabyn et al. (1993) and Buckley & Ward-Thompson (1996) conclude that this double-peak line profile comes from different clouds and suggest that a cloud–cloud collision is triggering the massive star formation in W49A. Wilner et al. (2001) found hot cores in the Welch ring, which are probably the precursors of UCHII regions. Alves & Homeier (2003) identified four massive stellar clusters based on the spatial distributions of the detected sources based on their ( $H-K_s$ ) colors, and they hypothesize that the W49 GMC collapsed to form the central massive cluster, and stellar winds and UV radiation triggered the surrounding the cloud to form the Welch ring. However, they concluded that there is no evidence of triggering for the other clusters on the south and east parts of the region. In addition, Peng et al. (2010) suggested that the triggering in the region is caused by expanding shells in the center of W49N. Recently, Gálvan-Madrid et al. (2013) studied the mass distribution in the whole GMC and concluded that it shows a hierarchical network of filaments at scales from  $\sim 10$  to 100 pc and suggested that the W49A starburst is formed from global gravitational contraction. They also concluded the feedback from the central young massive cluster is still not sufficiently strong to disrupt the GMC, and there is no evidence for significant disruption from photoionization.

Here we present *Spitzer* IRAC imaging and photometric analysis of the W49 star-forming complex with deep IR data from 1 to 24  $\mu\text{m}$  to investigate the massive YSOs (MYSOs) and embedded clusters forming around them. In Section 2 we describe the observations, data reduction techniques, and our near- and mid-IR source catalog and YSO classification. In Section 3 we present the clustering analysis, in Section 4 we present the SED fitting results for massive YSO candidates, in Section 5 we present the massive star formation tracers in the region, and in Section 6 we discuss the star formation history in W49 and compare it to other star-forming regions such as G305 and G333. Finally, in Section 7 we summarize our results and describe our future work.

## 2. OBSERVATIONS AND METHODS

### 2.1. IRAC Imaging

We assembled the mid-infrared *Spitzer*/IRAC observations of the W49 region obtained with the *Spitzer* IRAC instrument (Fazio et al. 2004) at 3.6, 4.5, 5.8, and 8.0  $\mu\text{m}$ . We list the dates and coordinates of each Astronomical Observation Request (AOR) in Table 1. The data are from several projects, including the following project IDs: 631 (PI: G. Fazio), 63 (J. Houck), 187 (GLIMPSE; E. Churchwell), and 80074 (Deep GLIMPSE; B. Whitney). The data set contained a total of 11,592 images with a frame time of 2 s. Also, we used a total of 1088 images acquired in 12 s High Dynamic Range (HDR) mode, which performs consecutive individual observations with exposure times of 0.4 and 10.4 s. Before performing the point-source detection and photometry, all the IRAC images were processed on an image-by-image basis using the routine *imclean*,<sup>6</sup> which is an IRAF<sup>7</sup> program for re-

**Table 1**  
Astronomical Observation Requests

AORKEY	Date (UT)	R. A. (J2000) (h m s)	Decl. (J2000) ( $^{\circ}$ ' ")	IRAC Reduction Pipeline ver.
7283968	2003 Oct 02	19:06:18	8:17:36	S18.25.0
4389888	2004 Apr 20	19:10:14	9:06:16	S18.25.0
11963904	2004 Oct 09	19:11:04	9:27:41	S18.25.0
11972096	2004 Oct 09	19:10:21	9:07:30	S18.25.0
11973376	2004 Oct 09	19:11:47	9:47:52	S18.25.0
11966976	2004 Oct 09	19:09:39	8:47:21	S18.25.0
11971072	2004 Oct 09	19:08:56	8:27:04	S18.25.0
11968768	2004 Oct 09	19:12:30	10:08:04	S18.25.0
11972864	2004 Oct 09	19:13:13	10:28:15	S18.25.0
11018240	2005 May 06	19:11:09	9:06:24	S18.25.0
11017984	2005 May 06	19:11:09	9:06:24	S18.25.0
45934848	2012 Nov 01	19:06:24	10:12:04	S19.1.0
45928960	2012 Nov 26	19:02:31	8:20:54	S19.1.0
45949952	2012 Nov 28	19:03:00	8:34:49	S19.1.0
45914880	2012 Nov 28	19:03:29	8:48:43	S19.1.0
45909248	2012 Nov 29	19:03:58	9:02:37	S19.1.0
45940224	2012 Nov 30	19:05:25	9:44:14	S19.1.0
45923328	2012 Nov 30	19:04:56	9:30:22	S19.1.0
45917184	2012 Nov 30	19:04:27	9:16:30	S19.1.0
45945600	2012 Nov 30	19:09:54	10:28:25	S19.1.0
45906176	2012 Dec 01	19:05:55	9:58:09	S19.1.0

moving the bright source artifacts (“pulldown,” “muxbled,” and “banding”; Hora et al. 2004; Pipher et al. 2004) from the Basic Calibrated Data (BCD) images.

Automated source detection and aperture photometry were carried out using PhotVis version 1.10 (Gutermuth et al. 2008). PhotVis utilizes a modified DAOPHOT (Stetson 1987) source-finding algorithm. Aperture photometry was performed with an aperture of  $2.4''$  radius and using a background annulus of inner and outer radii  $2.4''$  and  $7.2''$  respectively. Within an area of size  $\Delta l \times \Delta b = 1.68 \times 1.64$ , centered at  $(l, b) = (43.2, -0.02)$ , 332,442 sources were detected with IRAC photometry, and among these, 57,254 sources have photometry in all four IRAC filters. The photometric catalog is available in the electronic edition of this paper.

The individual BCD images (processed with the *Spitzer* IRAC pipeline version S18.25.0 and S19.1.0) were mosaicked into a larger image using the IRACproc package (Schuster et al. 2006). IRACproc is a PDL script based on the *Spitzer* Science Center’s post-BCD processing software MOPEX (Makovoz & Khan 2005), which has been enhanced for better cosmic-ray rejection. The full mosaic corresponds to a region with a size of approximately 360 by 360 parsecs at a distance of 11.1 kpc. The 5.8  $\mu\text{m}$  grayscale image of the entire mosaic can be seen in Figure 1 and a color image of the GMC with its surroundings can be seen in the left panel of Figure 2. We show the central region W49A in detail and the supernova remnant W49B in the right panel of Figure 2.

### 2.2. Completeness Estimate

We estimated the completeness in each IRAC channel by adding artificial sources of various magnitudes to a sample region (centered on 19:10:22, +9:07:35,  $1.5 \times 1.5$  in size). The artificial sources were added to the image using the observed IRAC point-spread function, scaled to the various magnitudes and added in a grid of positions in the image. We used the

<sup>6</sup> See <http://irsa.ipac.caltech.edu/data/SPITZER/docs/dataanalysis/tools/tools/continuity/continuity.html>

<sup>7</sup> IRAF is distributed by the National Optical Astronomical Observatories, operated by the Association of the Universities for Research in Astronomy, under a cooperative agreement with the National Science Foundation.

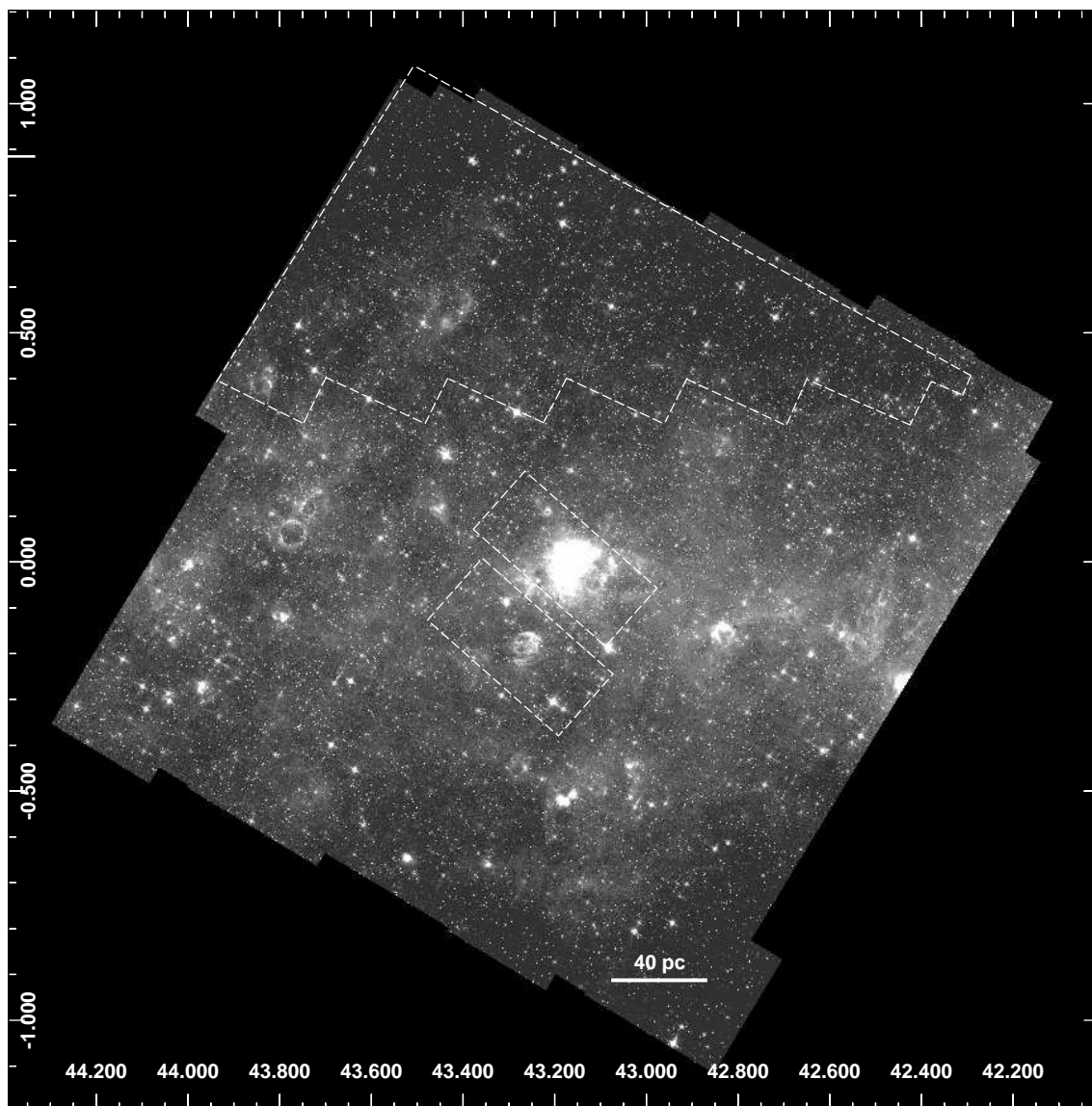


**Figure 1.**  $5.8\ \mu\text{m}$  grayscale image of the entire field analyzed in this study. Fields shown by the dashed boxes are where we have the deeper HDR images. The image is centered at  $l, b = 43.2, -0.02$ .

same source-finding and photometry routines previously described to extract magnitudes for sources in the field. We then compared the result to the input data to determine the completeness percentage and determined the photometric error for the artificial sources. The results of the completeness and error estimates are shown in Figure 3. The 90% completeness magnitudes for IRAC channels 1, 2, 3, and 4 are 15.1, 14.7, 12.35, and 12.12, respectively. The systematic error of the photometry was determined by the median value of the difference between the calculated photometric measurement of the point-spread function (PSF) source and its scaled magnitude and is plotted as a function of magnitude for each of the bands in Figure 3. Figure 4 shows the photometric errors as reported by the PhotVis photometry routine for the catalog sources. It can be seen in the  $5.8$  and  $8.0\ \mu\text{m}$  photometry error plots that the 12 s data provide smaller photometric errors, especially for magnitudes fainter than 12 mag.

### 2.3. Source Catalog

The source matching for the final catalog was performed in stages. First, all sources detected by *Spitzer* were matched

to Two Micron All Sky Survey (2MASS) Point Source Catalog (Skrutskie et al. 2006) sources by the PhotVis photometry routine. Since we have catalogs for mosaics based on short (2 s) and long (12 s) frames, we ran a band-merging process and took all sources from the short frames brighter than a certain cutoff (magnitude 9.6, 9.4, 7.5, and 7.2 for channels 1, 2, 3, and 4, respectively), which was chosen to be near but below the saturation limit of the 12 s frames.

Deep near-IR data are necessary, along with the IRAC photometry, in order to identify YSO candidates from other highly reddened objects and to more accurately fit models of their SEDs. Therefore, we used the UKIRT Infrared Deep Sky Survey, DR7PLUS (UKIDSS)<sup>8</sup> Galactic Plane Survey (Lucas et al. 2008) data, which are deeper and have better spatial resolution than those of 2MASS. We merged these data into our catalog using the TOPCAT software (Taylor 2005) pair match method with a maximum  $1''$  radial tolerance. We

<sup>8</sup> UKIDSS uses the UKIRT Wide Field Camera (Casali et al. 2007) on the United Kingdom Infrared Telescope, and the UKIDSS project is defined by Lawrence et al. (2007).



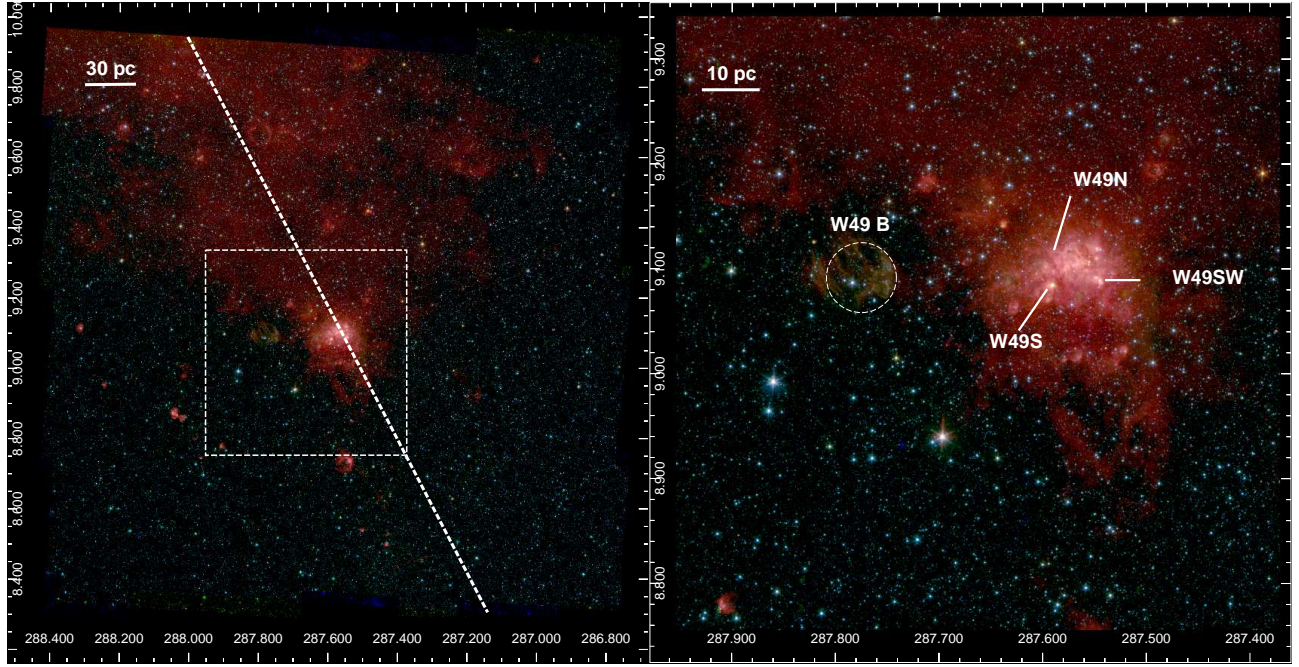


**Figure 2.** The left panel shows a color image of the entire mosaic in the *Spitzer* IRAC bands (blue:  $3.6\ \mu\text{m}$ , green:  $4.5\ \mu\text{m}$ , red:  $8.0\ \mu\text{m}$ ). The dashed line denotes the Galactic plane. The field shown by the dashed gray box is where we performed the clustering analysis, which is shown in detail in the right panel. The size scales in pc assume a distance to W49 of 11.1 kpc.

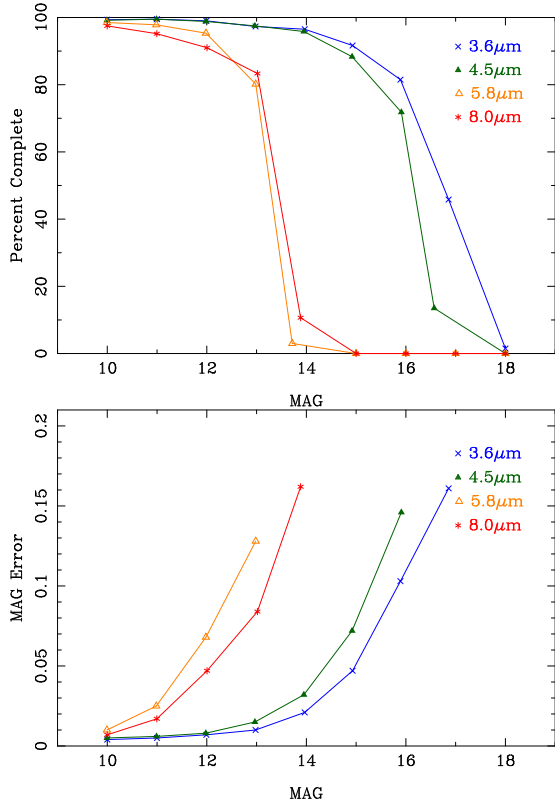


**Figure 3.** Top: estimate of the completeness of the IRAC data as a function of magnitude for the survey. Bottom: error estimate as a function of magnitude, derived from the completeness analysis.

adopted UKIDSS data, where they exist, for sources with 2MASS magnitudes fainter than the UKIDSS saturation limits, and 2MASS data otherwise (the UKIDSS cameras saturate near 12.65, 12.5, and 12 mag in  $J$ ,  $H$ , and  $K_s$ , respectively).

UKIDSS data have small uncertainties and small but mea-

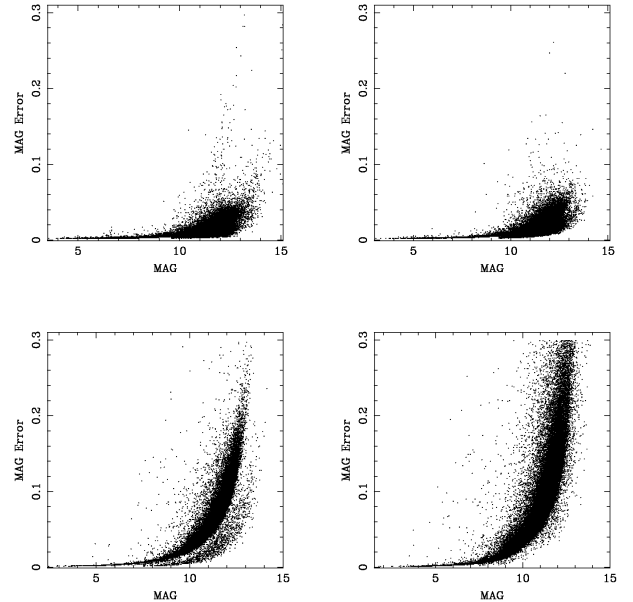


**Figure 4.** Uncertainty in magnitudes versus magnitude in the source catalog for the IRAC  $3.6$  (top left),  $4.5$  (top right),  $5.8$  (bottom left) and  $8.0\ \mu\text{m}$  (bottom right) bands. Sources with errors above  $0.3$  mag are not plotted.

surable zero-point photometric offsets from 2MASS. Therefore, we calculated the mean and standard deviations of the magnitude residuals between 2MASS and UKIDSS and applied a mean offset to UKIDSS data of  $0.02$ ,  $-0.09$ , and  $-0.04$  mag in  $J$ ,  $H$ , and  $K_s$ , respectively, to place them on the same system as the 2MASS photometry. Also, we found that the small photometric errors reported in the UKIDSS catalog (e.g.,  $<0.001$  mag for 13 mag sources) are probably unrealistic and have a detrimental effect on the source classification process. We therefore also adjusted the UKIDSS errors by adding  $0.02$  mag in quadrature to the values from the UKIDSS catalog before the source classification process.

**Table 2**  
Summary of Source Catalog

Band	Number of Sources
<i>J</i>	305,584
<i>H</i>	321,973
<i>K<sub>s</sub></i>	322,768
3.6 $\mu\text{m}$	310,485
4.5 $\mu\text{m}$	280,892
5.8 $\mu\text{m}$	93,896
8.0 $\mu\text{m}$	63,097
24.0 $\mu\text{m}$	2,268

**Table 3**  
Source-matching results

Catalog A	Catalog B	$r_{\text{match}}$	N. matches
IRAC	2MASS	1.0''	221,104
IRAC+2MASS	UKIDSS	1.0''	322,778
IRAC+(2MASS/UKIDSS)	MIPS	2.0''	2268

This imposes an error floor of 0.02 mag but does not affect the larger errors. We also used the MIPS GAL Archive 24  $\mu\text{m}$  data (Gutermuth & Heyer 2015) and added them to our catalog by using the TOPCAT software pair match method with a maximum 2'' radial tolerance (since the resolution of the MIPS 24  $\mu\text{m}$  band is 6'' FWHM, the position errors can be higher than IRAC). Also, we eliminated the bad matches when they are not identified as point sources in MIPS image (see Section 2.4). Our final catalog therefore contains photometry of sources over a wavelength range from 1.2 to 24  $\mu\text{m}$ . A summary of the source catalog and source-matching results can be found in Table 2 and in Table 3, respectively. The source catalog itself is presented in Table 5.

#### 2.4. YSO Classification

In this study we used the selection method based on the color and magnitude criteria defined in Gutermuth et al. (2009). This method uses flux ratios or colors to identify YSO candidates. This method is an updated version of that introduced by Gutermuth et al. (2008). Gutermuth et al. (2008, 2009) showed that the  $K_s$ -[3.6] vs. [3.6]-[4.5] color-color diagram is one of the best diagnostics for identifying and classifying YSOs. The *J* and *H* bands allow us to further extend the SED and sort out YSO candidates from highly reddened main-sequence stars and other background objects. With the near-IR and *Spitzer* bands, we can quickly identify YSO candidates and determine their evolutionary status. We classify the YSOs into the categories of Class I sources (protostars with circumstellar disks and infalling envelopes) and Class II sources (pre-main-sequence stars with optically thick disks). In addition to these classes, “deeply embedded sources,” which are Class I sources with bright emission at 24  $\mu\text{m}$ , and “transition disks,” which are Class II sources with significant dust clearing within their disks, can be identified with this method.

To identify the YSOs in W49, we first applied the Gutermuth et al. (2009) criteria to the 332,442 point sources in our catalog. First, we separate out extragalactic contaminants such as star-forming galaxies, broad-line active galactic nuclei (AGNs), and polycyclic aromatic hydrocarbon (PAH) rich galaxies. Following Gutermuth’s criteria, star-forming

galaxies are classified from very red 5.8 and 8.0  $\mu\text{m}$  colors (Stern et al. 2005) because of their strong PAH feature emission. The [4.5] – [5.8] versus [5.8] – [8.0] and [3.6] – [5.8] versus [4.5] – [8.0] color-magnitude diagrams and a combination of 8 different conditions based on all four IRAC bands are used to identify the star-forming galaxies and PAH galaxies. Broad-line AGNs have mid-IR colors that are largely consistent with YSOs (Stern et al. 2005). Therefore, the AGNs are classified by using the [4.5] versus [4.5] – [8.0] color-magnitude diagram and a combination of six different conditions involving these two IRAC bands.

We remove knots of shock emission and sources contaminated by PAH emission using the [4.5] – [5.8] versus [3.6] – [4.5] color-color diagram and seven different conditions involving these three IRAC bands. Class I YSOs are identified using the same diagram and a combination of two conditions that show their discriminant colors. Finally, we extract the Class II YSOs from the remaining objects in the catalog using the [4.5] – [8.0] versus [3.6] – [5.8] color-color diagram and a combination of four different conditions involving all four IRAC bands.

With the application of each step of the full Gutermuth contaminant object identification criteria, we selected a total of 4 candidate broad-line AGNs, 53 PAH-rich galaxies, 11 knots of shocked gas emission, and 639 PAH-contaminated apertures, which are shown in Figure 5.

After removing all these contaminants, the second step in the Gutermuth et al. (2009) method is to classify the YSOs with near-infrared data, and the third step is to reexamine the entire catalog with MIPS 24  $\mu\text{m}$  photometry. After we applied the full set of criteria, we ended with 73 deeply embedded near-infrared objects, 271 Class I YSOs, 3021 Class II YSOs, and 231 transitional disk candidates.

In our analysis of the W49 data we had to take into account its greater distance and the possible higher level of contamination from objects such as AGB stars, background sources, and other extragalactic contaminants that have probably been classified as YSOs. Since AGB stars are bright and, in general, slightly bluer than YSOs (Robitaille et al. 2008; Koenig & Leisawitz 2014), we considered the bright YSOs that also follow the following selection criteria as candidate AGB stars:

$$3 < [3.6] < 9.5 \text{ and } 0.2 < [3.6] - [4.5] < 1.25$$

or

$$3.5 < [3.6] < 9.5 \text{ and } 0.4 < [3.6] - [8.0] < 2.6$$

The large cluster of objects at bright magnitudes in [3.6] – [4.5] versus [3.6] and [3.6] – [8.0] versus [3.6] color-magnitude diagrams are consistent with being AGB stars. With this criterion we classified 212 sources as candidate AGB stars.

The Gutermuth et al. (2009) criteria require detections at 5.8 or 8.0  $\mu\text{m}$  to identify extragalactic and background contaminants, and we have only 57,254 sources detected in all four IRAC bands. Therefore, for the rest of the sources that have been classified as YSO candidates in Phase II and have only IRAC 3.6 and 4.5  $\mu\text{m}$  photometry, we had to think about possible extragalactic contaminants. Thus, we applied a selection cut of [3.6] = 13 mag to separate YSO candidates from potential background/foreground objects. However, at the distance to W49 that would also remove up to 90% of the low-mass YSOs that we are otherwise sensitive enough to detect. We report these additional YSO candidates separately to

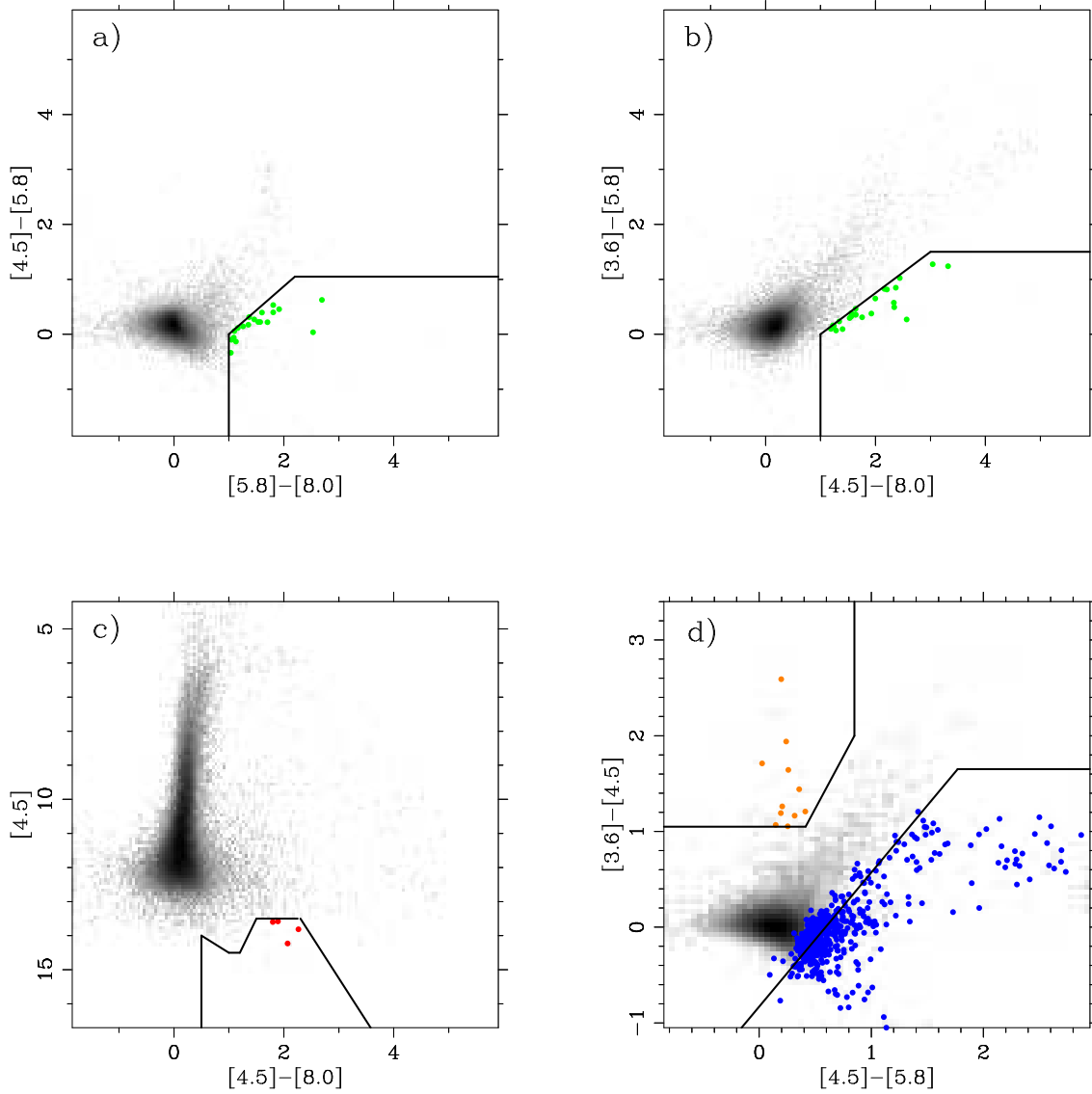


**Figure 5.** Color-color and color-magnitude diagrams used to identify contaminant objects among the sources with detection at all four IRAC bands following the criteria in Gutermuth et al. (2009). The background logarithmic gray scale indicates the overall source density in each color-color and color-magnitude space. In panels (a) and (b), PAH galaxies are marked with green circles. In panel (c), candidate AGNs are marked by red circles. Panel (d) shows knots of shocked emission (orange circles) and PAH-contaminated sources (blue circles).

denote the lower confidence in their identification but do not remove them from our catalog. With this criterion we flagged 64 Class I, 1932 Class II, and 75 transition disk candidates with a “uc” mark in our catalog, as shown in Table 5, and called them faint YSO candidate sources. These faint YSO candidate sources will not be used in the analysis described in Section 3.

As a final step, we examined the regions near the YSO candidate objects and eliminated 74 transition disk and 27 embedded source candidates if they did not appear as point sources in the MIPS  $24\ \mu\text{m}$  images, seem like an artifact around a very bright source, or are significantly more extended than the FWHM for the  $24\ \mu\text{m}$  PSF.

The color-color diagrams of the identified YSOs are shown in Figure 6 and the color-color diagrams combining MIPS and IRAC photometry and eliminated AGB star candidates and faint YSOs are shown in Figure 7. The points are plotted without dereddening their photometry.

We also determined the slope of the SEDs in the mid-IR and

examined the resulting class distribution of YSOs. The class identification for the slope of  $\log(\lambda F_\lambda)$  vs.  $\log(\lambda)$  between 2 and  $\sim 20\ \mu\text{m}$  from Lada (1987) is

$$\alpha \geq 0.3 \text{ Class I}$$

$$0.3 > \alpha \geq -0.3 \text{ Flat Spectrum}$$

$$-0.3 > \alpha \geq -1.6 \text{ Class II}$$

$$-1.6 > \alpha \geq -2.7 \text{ Class III}$$

In Figure 8, we show the identified YSO candidates with the distribution of their SED spectral index. The embedded sources have mainly positive spectral slopes, similar to Class I YSOs. Most of the IRAC-identified Class I YSO candidates are found to have positive spectral index, indicating substantial infrared excess and confirming their identification as early stage YSOs. The IRAC-identified Class II YSOs are mainly grouped in the CII region as shown in Figure 8, consistent with the classification according to the Gutermuth et al.



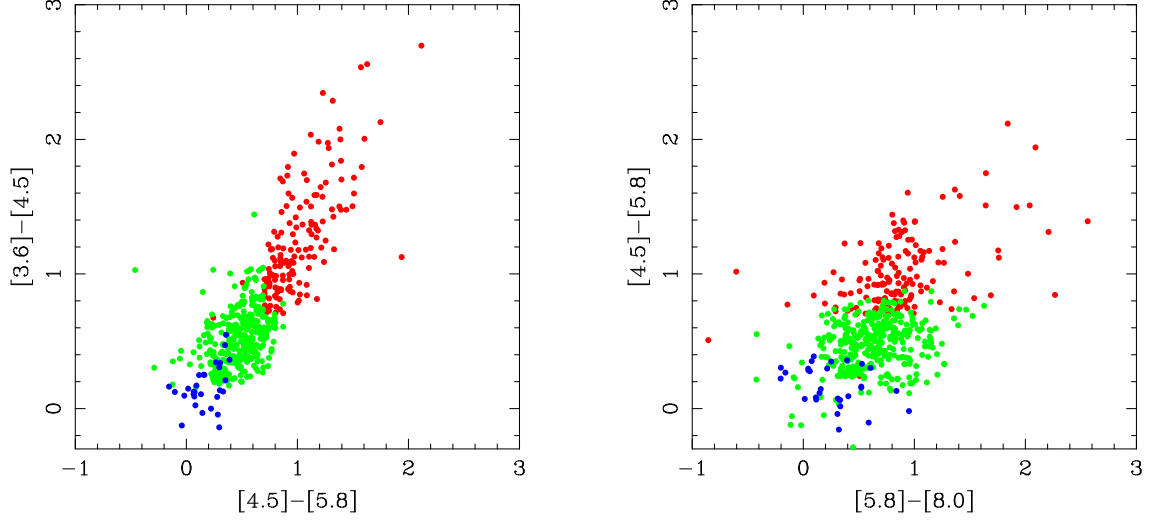


**Figure 6.** IRAC color-color diagrams used for identifying YSO candidates in W49. Left:  $[3.6] - [4.5]$  vs.  $[4.5] - [5.8]$ ; right:  $[4.5] - [5.8]$  vs.  $[5.8] - [8.0]$ . In both panels, red points are Class I, green points are Class II, blue points are transition disk candidates.

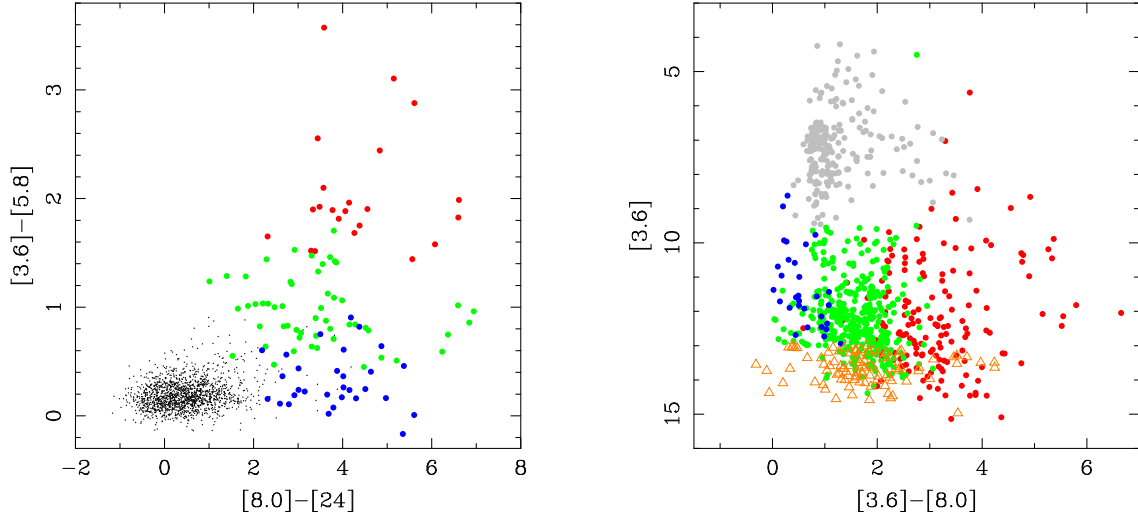


**Figure 7.** IRAC and MIPS color-color diagrams used for eliminating the AGB stars and faint objects that could be background/foreground contamination. Left:  $[3.6] - [5.8]$  vs.  $[8.0] - [24]$ ; right:  $[3.6]$  vs.  $[3.6] - [8.0]$ . The red points are Class I; green points are class II; blue points are transition disk candidates; black points are class III and photospheres; gray points are AGB star candidates; and orange points are faint YSO candidates.

(2009) method. The slope distribution for transition disk candidates agrees with these sources being evolved YSOs.

The full list of objects in Table 5 includes their classification (if available) and SED spectral index. In Table 4 we summarize the final source classification results.

### 2.5. Comparison with WISE

We assembled the *WISE* data for the W49 region from the AllWISE Data Release (Cutri et al. 2013) and used the YSO selection method that is based on color and magnitude criteria defined in Koenig & Leisawitz (2014). We compared these data with the *Spitzer* catalog using the source positions, considering objects a match if the distance between the *WISE* and *Spitzer* sources was less than  $6''$ . Nearly half of the IRAC YSOs did not have any match in the *WISE* point-source catalog. Most of the IRAC YSOs that did not have corresponding entries in the *WISE* catalog are faint or unresolved in *WISE*. This includes the central portion of W49, where the source density is too high given the resolution of *WISE* to allow point-source detection among the bright nebular backgrounds. In the small number of overlapping sources, there

are no obvious trends that explain all of the differences in classification. Overall, *WISE* channel 1 measurements are a bit dimmer for all the YSOs than the IRAC channel 1 measurements. The IRAC channel 2 vs. *WISE* channel 2 has a lot of scatter (differences up to about 0.5 mag), but they look more centered around 0. The correspondence between the longer *WISE* and *Spitzer* wavelengths is not as close, but the YSOs appear much brighter at long wavelengths according to *WISE* than the *Spitzer* values. This effect could be due to the larger *WISE* beam and other sources or extended emission being included in the *WISE* photometry of the YSOs.

We found that a total of 47 *WISE* YSOs (25 Class I and 22 Class II) match to IRAC point sources. However, only 20 of them match to the IRAC YSOs within  $50''$  of the center of W49, shown in Figure 9. Within this group of 20 *WISE* YSOs, 12 Class I candidates match IRAC Class I candidates, 1 *WISE* Class I candidate matches an IRAC Class II candidate, 5 *WISE* Class II candidates match IRAC Class II candidates, and 2 *WISE* Class II candidates match IRAC Class I candidates. The rest of the *WISE* YSO candidates (27 sources) match to IRAC

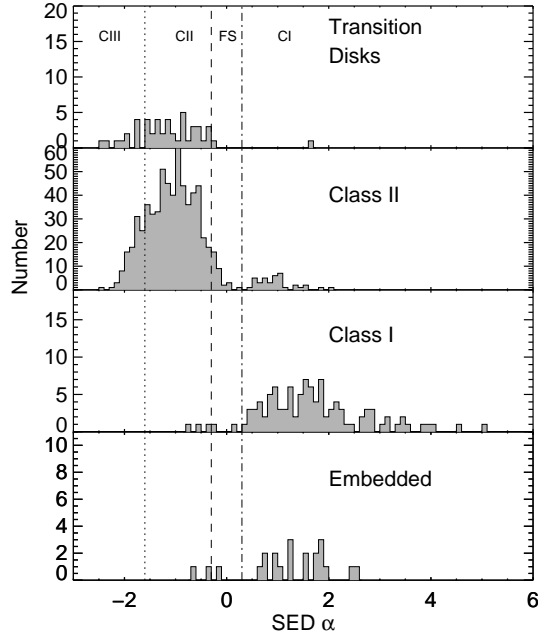


**Figure 8.** Distribution of the SED spectral index  $\alpha$  for sources identified as YSO candidates. The three vertical lines mark the division between the YSO regions based on their SED slopes. From left to right: Class II, flat spectrum, and Class I.

**Table 4**  
Source Classification Summary

Class	Number of Objects
Class I	186
Class II	907
Transition disks	74
Embedded protostars	46
Faint Class I*	64
Faint Class II*	1932
Faint transition disk*	75
Photospheres	247,142
AGB candidates	212
Other**	705
Unclassified	81,097
Total	332,442

\* These are the YSO candidates with lower confidence.

\*\* Includes PAH-emission dominated sources, shocked-gas-emission-dominated sources, broad-line AGN candidates, and PAH galaxy candidates. Unclassified sources lack detection in four bands (either  $HK_s$ , IRAC 1 and 2, or IRAC 1, 2, 3 and 4) or a bright MIPS  $24\ \mu\text{m}$  detection.

AGB stars, photospheres, or PAH-contaminated source candidates. The list of *WISE* YSOs that match with IRAC YSOs is given in Table 6 and the sources are shown on an  $8.0\ \mu\text{m}$  grayscale image in Figure 9.

The source classification with *WISE* data indicates that the high density of sources in the central region, saturation, and source confusion prevent us from identifying YSO candidates. Differences in classification may also originate from the inaccurate photometry and lead us to identify some contaminant sources as YSO candidates with the *WISE* data. Because of these effects, we conclude that the *WISE* data are not very useful at identifying YSO candidates in the central part of W49, and therefore we did not include *WISE* YSO candi-

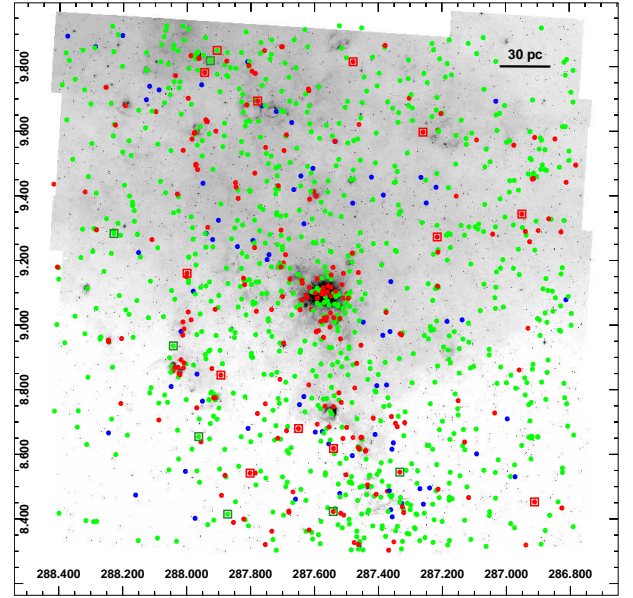


**Figure 9.** IRAC and *WISE* YSO candidate distribution overlaid on the IRAC  $8\ \mu\text{m}$  image. The IRAC YSOs are shown with the filled circles, with red for Class 0/I, green for Class II, blue for transition disks. The *WISE* YSO candidates are plotted as boxes, with red for *WISE* Class I and green for *WISE* Class II.

dates in our further analysis. This conclusion may apply to other regions that are similarly distant or have a high density of sources.



**Table 5**  
Source List

Source Name <sup>a</sup>	R.A. J2000.0 (°)	Decl. J2000.0 (°)	<i>J</i> (mag)	<i>H</i> (mag)	<i>K<sub>s</sub></i> (mag)	[3.6] (mag)	[4.5] (mag)	[5.8] (mag)	[8.0] (mag)	[24] (mag)	Type <sup>b</sup>	Phase <sup>c</sup>	Flag <sup>d</sup>	SED slope $\alpha$
SSTOERC_G043.0997-00.0296	287.56134	9.02556	19.74(15)	17.04(03)	15.54(03)	...	12.27(08)	...	...	4.04(10)	0	0	...	1.51
SSTOERC_G042.6828+00.2115	287.15012	8.76694	17.13(02)	16.03(02)	14.90(02)	11.56(02)	10.37(01)	9.04(02)	8.18(02)	...	1	1	...	1.88
SSTOERC_G042.2532+00.1846	286.97418	8.37315	16.44(02)	14.80(02)	14.08(02)	13.03(05)	12.44(05)	11.70(09)	10.95(11)	7.5(09)	2	1	...	-0.47
SSTOERC_G042.8060+00.6517	286.81198	9.07888	13.95(02)	13.08(02)	12.68(02)	12.35(03)	12.21(02)	11.91(10)	11.31(11)	8.30(09)	3	1	...	-1.72
SSTOERC_G043.2857-00.5262	288.09421	8.96086	18.83(06)	17.12(04)	16.10(03)	14.62(14)	13.71(09)	...	...	...	1	3	uc	0.20
SSTOERC_G043.1518-00.9278	288.39154	8.65611	15.53(02)	14.94(02)	14.31(02)	13.93(06)	13.20(18)	...	...	...	2	3	uc	-1.93
SSTOERC_G042.4240+00.1903	287.04852	8.52740	15.81(02)	14.59(02)	13.96(02)	13.35(07)	13.36(09)	...	...	8.27(10)	3	3	uc	-0.87
SSTOERC_G042.5060+00.5319	286.78003	8.75746	17.55(01)	15.56(02)	14.67(02)	13.84(03)	13.91(03)	13.44(11)	...	...	99	1	...	...
SSTOERC_G042.7282+00.4616	286.94656	8.92236	...	18.70(14)	17.30(09)	14.55(13)	13.64(08)	12.40(13)	11.55(12)	...	29	0	...	...
SSTOERC_G042.9654+00.6453	286.89200	9.21747	15.85(02)	13.88(02)	13.02(02)	12.33(01)	12.43(02)	10.51(05)	12.18(13)	...	19	0	...	...
SSTOERC_G042.8351+00.3941	287.05713	8.98614	5.62(02)	5.09(05)	4.88(03)	6.64(01)	4.93(00)	4.90(00)	4.85(00)	...	9	0	...	...
SSTOERC_G042.8251+00.6911	286.78540	9.11397	14.91(02)	12.76(02)	11.83(02)	11.24(01)	11.43(01)	11.03(05)	11.04(06)	...	20	0	...	...
SSTOERC_G043.1583+00.8687	286.78085	9.49150	17.29(03)	13.29(02)	10.26(02)	6.48(00)	5.75(01)	3.87(00)	...	...	12	3	...	...
SSTOERC_G042.8033+00.6849	286.78085	9.09181	17.43(03)	16.15(03)	15.60(03)	14.79(12)	14.28(12)	...	...	...	4	3	...	...

**Note.** — Table 5 is published in the electronic edition of the *Astrophysical Journal*. A portion is shown here for guidance regarding its form and content. Values in parentheses signify error in last 2 digits of magnitude value. Right ascension and Declination coordinates are J2000.0.

<sup>a</sup> Sources are named according to their Galactic longitude and latitude with the prefix SSTOERC, referring to Spitzer Space Telescope, Origin and Evolution of Rich Clusters project.

<sup>b</sup> 0; deeply embedded, 1; Class I, 2; Class II, 3; transition disks, 99; Class III and photospheres, 9; shocked gas emission, 29; AGNs, 19; PAH galaxies, 20; PAH dominated sources, 12; AGBs, -100; unclassified.

<sup>c</sup> Sources are flagged according to the phase they were classified. 1; Gutermuth et al. (2009) classification Phase I, 2; Phase II, 0; Phase III, 3; our AGBs, faint YSO/background contamination phase (see Section 2.4).

<sup>d</sup> YSO candidates near a bright IRAC source within 35'' are flagged with a question mark. Faint YSOs which can be background/foreground contamination are flagged with the letter "uc".

### 3. CLUSTERING ANALYSIS

#### 3.1. Spatial Distribution of YSOs

Figure 9 shows the spatial distribution of the YSOs overlaid on the 8.0  $\mu\text{m}$  grayscale image of the region. The sources are colored according to their evolutionary class: blue for transition disks, green for Class II, and red for Class 0/I candidates. In the central W49A region, it is clear that Class 0/I sources and Class II sources are clustered together. In the whole region, however, the Class 0/I sources are clustered, or in filamentary form, while the Class II sources are more evenly distributed.

#### 3.2. Minimal Spanning Tree (MST)

To understand the star formation history in W49 and compare W49 to other star-forming regions, we want to identify individual groups or clusters of YSOs and compare their properties such as sizes and ages. In order to find the clusters, we used a method called MST (Cartwright & Whitworth 2004), which uses the spatial distribution of sources to determine a cluster membership without any kinematic information.

The MST method defines clusters as a collection of stars that are connected to each other by branches smaller than the cutoff distance ( $d_c$ ) or branch length and with a minimum number of stars ( $N$ ) in a group. It has been a popular tool in recent years and has been used for many nearby star-forming regions (Koenig et al. 2008; Gutermuth et al. 2009; Beerer et al. 2010; Billot et al. 2011; Chavarría et al. 2014). However, there is no unique way to determine a cutoff distance for a cluster determination.

The most common way used for nearby regions is to plot the distribution of cutoff distances, fit straight lines through the long and short cutoff distance domains, and choose the point of intersection (Gutermuth et al. 2008). Choosing a cutoff distance that falls between these two domains is also a good way to separate clusters from distributed sources (Gutermuth et al. 2008, 2009). With this method, Beerer et al. (2010) determined the cutoff distance as 61'' (0.43 pc) for the Diamond Ring region in the Cygnus-X star-forming complex, which is at a distance of 1450 pc. On the other hand, Guarcello et al. (2013) derived the cutoff distance as 72'' (0.51 pc) for the Cygnus-OB2 region in the Cygnus-X complex. All these values are smaller than the 88'' (0.86 pc) derived by Koenig et al. (2008) for the W5 star-forming region, which lies at a distance of 2 kpc, which may indicate that Cygnus-X is more densely populated with YSOs than W5.

Chavarría et al. (2014) used the MST method for nearby embedded star-forming regions by dividing each region according to their YSO concentrations. For W5-east they found an average cutoff distance of 33'' (0.32 pc), which is different than the 88'' (0.86 pc) that was found by Koenig et al. (2008) for the whole of W5. Billot et al. (2011) used the MST method according to the definition given in Gutermuth et al. (2009) for Galactic star-forming regions like W43 and VulOB1 to derive their clustering properties and found cutoff distances of  $\sim 80''$  (corresponding to 4.3 pc at the distance of W43) and  $\sim 100''$  (5.4 pc), respectively. These cutoff distance differences may be partly a resolution effect, since at greater distances multiple stars may blend into single objects, and fewer stars are detected owing to corresponding lower sensitivity in the more distant regions. Low-resolution observations of distant star-forming regions probe only larger-scale structures, and it is hard to see the hierarchical substructure in these regions. In addition to Galactic regions, the MST

method has been used by Bastian et al. (2007) for the star-forming regions in the M33 galaxy. In order to prevent an artificial length scale according to the resolution limit and seeing a large number of stars as blended or as single sources, they used cutoff distances from 5'' to 65'' (corresponding to 19 to 252 pc assuming the distance of M33 as 800 kpc) in 13 equal steps. Examining the clustering at the different values allowed them to see all levels of hierarchy in M33.

##### 3.2.1. W49 Clustering Analysis with MST Method

To compare with previous clustering analysis in nearby star-forming regions, we first use the straight-line fit method to determine the branch length cutoff for W49. We plot the number of clustered objects versus branch length. Branch lengths between 82'' and 130'' deviated significantly from linearity, so we masked these areas and found the intersection to the best fits to the long and short branch length regimes. We found a cutoff distance of 96'', which corresponds to 5.2 pc at 11.1 kpc, similar to the cutoff distance found by Billot et al. (2011) for W43 and VulOB1. However, this cutoff distance shows that the straight-line fit method does not find the isolated subclusters, instead picking up almost the whole star-forming region with a diameter of 27 pc associated with the overdensity of YSOs.

To determine the statistical significance of the W49 clusters identified with this cutoff distance, we performed simulations to examine the clustering properties of randomly distributed objects. We created 1000 distributions of 231 objects spread randomly in a 0.5 x 0.5 degree field to match the number of YSOs and the size of the central region of W49. We examined the number of groups that would occur in a random distribution as a function of the minimum group size. We chose the minimum group size that gave the fewest random groups for a given branch length.

We found that for a cutoff distance of 96'' and a minimum group size  $N = 7$ , our random distribution of YSOs will yield on average nine groups or subclusters. We looked at the group with the highest number of members in each simulation and found that these largest groups had an average of  $22 \pm 6$  members, with a maximum of 78. For our observed distribution we see a much smaller number of clusters, finding three concentrated groups of YSOs containing 52% of the observed sources using a 96'' cutoff distance. The population of the largest observed group (Cluster 1, G43.15–0.01) is 97, significantly higher than the maximum seen in simulated random distributions. Cluster 2 (G43.33–0.08) has 15 members, similar to the  $16 \pm 2.9$  average size of observed for random distributions of objects. Cluster 3 (G43.31–0.20) has nine members, slightly smaller than the  $13 \pm 2.0$  found for the third-largest random subcluster. The remaining 110 YSOs (48%) did not belong to any of these clusters and are considered to be part of the distributed population.

The identified clusters in W49 are shown in the left panel of Figure 11 and their properties are summarized in Table 7. The distribution of cutoff distances versus the number of sources is plotted in the left panel of Figure 10. To see how the numbers of groups change according to the cutoff distance, we plotted the number of groups containing seven or more stars versus cutoff distance from 1'' to 300'', with steps of 1'', in the right panel of Figure 10.

This comparison indicates that the largest group observed, cluster 1, is likely formed from the extended YSO population of W49, representing a large-scale structure extending 26.86 pc in diameter. The lower-density clusters 2 and 3 ob-

**Table 6**  
WISE YSO Source List

WISE R.A. ( $^{\circ}$ )	WISE Decl. ( $^{\circ}$ )	W1 (mag)	W2 (mag)	W3 (mag)	W4 (mag)	WISE Class <sup>a</sup>	Matched IRAC Source Name	IRAC Class <sup>a</sup>
287.2152079	9.2737751	14.05(21)	12.36(07)	8.90(04)	5.99(06)	1	SSTOERC G043.1622+00.3880	1
287.4789811	9.8163322	12.33(06)	9.93(03)	5.45(02)	2.05(02)	1	SSTOERC G043.7637+00.4076	1
287.2595223	9.5982765	13.05(07)	11.38(04)	8.83(07)	5.70(05)	1	SSTOERC G043.4703+00.4988	1
286.9496205	9.3442128	11.55(09)	10.27(02)	6.91(02)	3.95(02)	1	SSTOERC G043.1041+00.6530	1
287.8935132	8.8461252	10.48(03)	9.07(02)	6.72(04)	4.48(05)	1	SSTOERC G043.0923-00.4037	1
287.9997854	9.1612432	11.48(03)	9.66(02)	7.24(04)	4.84(03)	1	SSTOERC G043.4202-00.3508	1
287.7786347	9.6947734	11.65(05)	9.5(03)	5.90(02)	2.43(02)	1	SSTOERC G043.7923+00.0895	1
287.9451674	9.7828376	12.20(05)	10.68(03)	7.48(05)	3.98(05)	1	SSTOERC G043.9462-00.0153	1
287.5414301	8.4239783	11.63(03)	10.60(03)	8.12(05)	5.34(04)	2	SSTOERC G042.5570-00.2899	1
287.5407128	8.6191474	11.04(03)	9.32(02)	6.11(02)	3.85(03)	1	SSTOERC G042.7298-00.1991	1
287.3331588	8.5458962	10.43(02)	9.22(02)	7.06(03)	5.73(08)	2	SSTOERC G042.5701-00.0509	1
286.9115172	8.4531359	11.19(04)	9.62(02)	7.06(02)	4.80(05)	1	SSTOERC G042.2956+00.2765	1
287.6502571	8.6810581	9.53(02)	6.61(02)	4.13(01)	1.76(02)	1	SSTOERC G042.8347-00.2668	1
287.8018156	8.5427571	9.17(02)	7.29(02)	5.20(01)	3.90(02)	1	SSTOERC G042.7814-00.4635	1
288.0424475	8.9366108	9.34(02)	8.89(02)	7.68(03)	5.34(06)	2	SSTOERC G043.2406-00.4921	2
287.9274058	9.8193046	9.70(02)	8.85(02)	6.37(02)	4.02(03)	2	SSTOERC G043.9705+00.0170	2
287.9060792	9.8514046	11.08(03)	9.68(02)	7.47(04)	4.74(06)	1	SSTOERC G043.9892+00.0504	2
288.2291642	9.2840378	11.59(04)	10.46(04)	8.25(05)	5.49(05)	2	SSTOERC G043.6338-00.4946	2
287.8718301	8.4157962	11.98(03)	11.13(03)	8.81(06)	6.18(06)	2	SSTOERC G042.7008-00.5836	2
287.9626502	8.6556335	12.02(04)	11.61(04)	9.01(09)	5.90(07)	2	SSTOERC G042.9550-00.5526	2

<sup>a</sup> 0: deeply embedded; 1: Class I; 2: Class II candidate sources.

served with the straight-line fit cutoff distance of 96'' have a higher probability of occurring randomly as a result of chance alignment of distributed YSOs.

To investigate the substructure within these clusters, we also investigated the number and size distribution of subclusters identified as a function of the cutoff distance used. For a random distribution, the number of groups identified in the minimum spanning tree is a function of both the minimum group size and the cutoff distance. A long cutoff distance and small minimum group size will break the MST into a large number of small, more dispersed clusters. We examined the number and size distributions of clusters that would arise in a randomly distributed population of YSOs to find the cutoff distance and minimum group size that yielded the largest number of groups that had a low probability of occurring randomly.

We found that using a break length of 40'' (2.2 pc in W49) and requiring  $N \geq 6$  or more members isolates seven subclusters, a distribution that did not occur in the 1000 simulated randomly distributed trials. Only 8.8% of the random trials had at least one group of six or more members, and only 0.3% of the random YSO distributions had two groups, with no trials having more than two random groups. Therefore, the random trials indicate that the identified subclusters likely represent physically associated groups of YSOs, with a  $< 10\%$  likelihood that one of the subclusters could be a random association. Note also that the subclusters identified are all within the three clusters identified with the larger break length and minimum cluster member number. However, owing to the complex line of sight toward W49, without additional data to determine the distance to each object, we cannot rule out the possibility that all of the clusters may not all be at the same distance as the W49 GMC.

According to the YSO clustering analysis, identified subclusters in W49 have sizes of order a few parsecs in diameter with six to nine sources in each subcluster. On the other hand, subclusters identified in the Cygnus-X DR21 region have 10–148 sources with diameters of 1–8.1 pc (Beer et al. 2010). The same study finds subclusters in the AFGL 2636 re-

gion with diameters of 1.1–3.6 pc with 12–149 sources. Similarly, Koenig et al. (2008) found subclusters in the W5 region with 10–201 sources with diameters of a few parsecs. W49 has smaller clusters with less members; however, this might be a result of incompleteness. It also should be noted that these studies used different criteria in their subcluster analyses. To compare W49 to other previously observed regions, in Section 6.3 we examine the clustering properties of the star-forming regions G305 and G333 with the same method used for W49 (after rescaling to account for their different distances) and then compare their clustering properties in detail.

The properties of each W49 subcluster are shown in Table 8, and subclusters are shown in the right panel of Figure 11. All identified groups and clusters from both large and small cutoff distances can be seen in Figure 12 and the summary of the results can be seen in Table 9, with the physical scale assuming that the clusters are at 11.1 kpc.

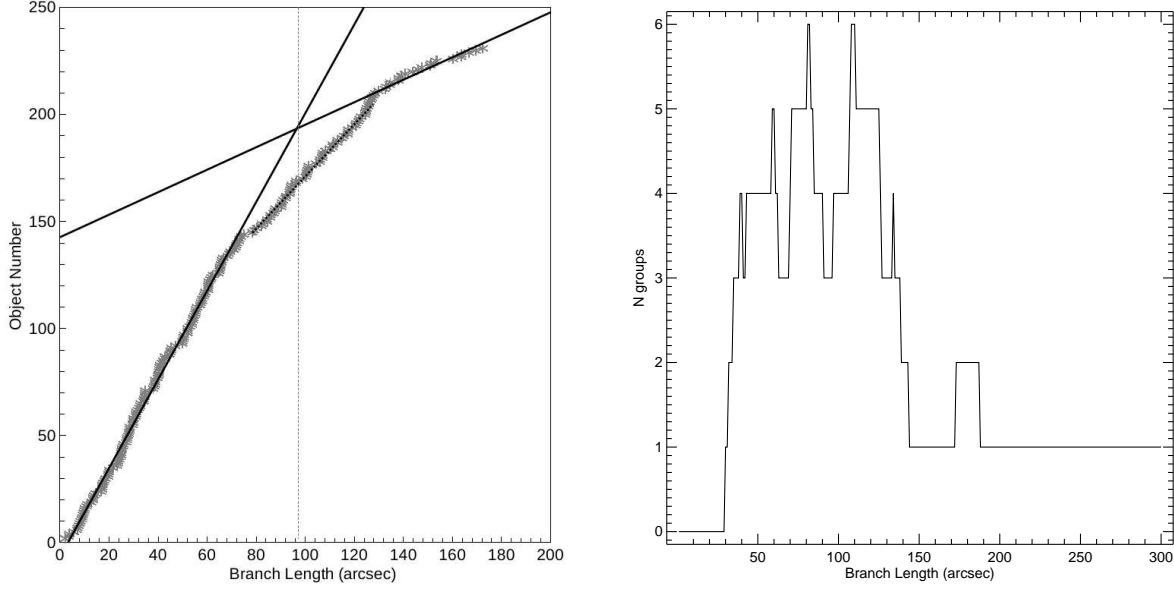
### 3.2.2. YSO Densities in Clusters

Figure 13 shows the YSO nearest-neighbor distance in the whole cloud complex, with the YSO candidates in identified clusters overlayed on each panel. The YSO nearest-neighbor distance grayscale images show the YSO nearest-neighbor distance in arcseconds, with white regions being higher density. Panel (a) shows the plots with the YSO candidate population, and Panel (b) shows the same maps but includes the faint YSOs/possible contaminant sources. It can be seen in Panel (b) that there is an overdensity of faint YSOs at the position of W49B, potentially indicating an associated low-mass star cluster, although it could be a chance alignment.

## 4. SED MODELS OF MYSOS

We have applied an SED fitting method described in Azimlu et al. (2015) to the 231 YSO candidates in the MST clusters in order to identify the most massive candidates in our sample and obtain a rough estimate of their properties. The most common method to find an SED model is to compare the models to data points, find the  $\chi^2$  value using the photometric errors, and pick the model that minimizes the  $\chi^2$ .





**Figure 10.** Left: The MST branch length distribution. The straight lines represent the linear fit to the points smaller and larger than the chosen branch length. The point of intersection  $d_c = 96''$ , and the minimum number of stars  $N = 7$ . Right: Number of groups containing seven or more stars identified by the MST algorithm.

**Table 7**  
Properties of the Clusters in W49 GMC for  $d_c = 96''$

No.	Cluster Name	R.A. (J2000.0) ( $^{\circ}$ )	Decl. (J2000.0) ( $^{\circ}$ )	$N_{IR}^a$	I	II	II/I <sup>b</sup>	$N_{emb}^c$	$N_{td}^d$	Diameter ( $''$ )	Diameter (pc)
1	G43.15-0.01	287.56496	9.074502	97	31	57	1.84(0.41)	9	0	497.88	26.86
2	G43.33-0.08	287.71438	9.202276	15	2	10	5.00(3.87)	1	2	244.17	13.17
3	G43.31-0.20	287.808112	9.134392	9	2	7	3.50(2.81)	0	0	176.38	9.52

<sup>a</sup> Number of stars with infrared excess. Includes Class I, Class II, deeply embedded protostars, and transition disk candidates.

<sup>b</sup> Number in parentheses indicates Poisson uncertainty in ratio.

<sup>c</sup> Number of deeply embedded protostars.

<sup>d</sup> Number of transition disk candidates.

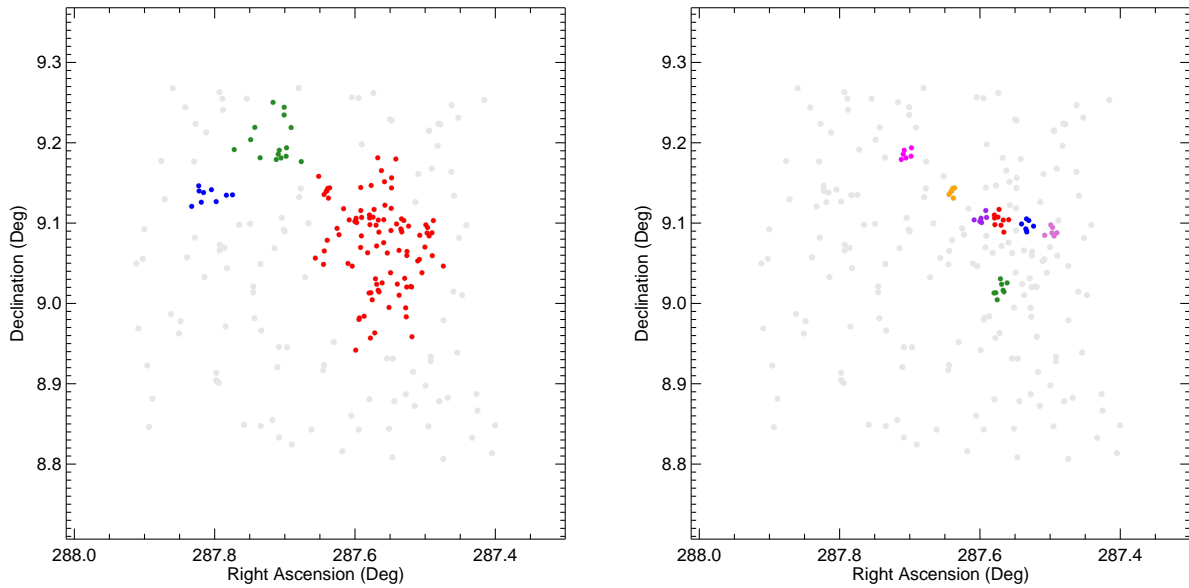


**Figure 11.** Left: three MST clusters in the W49 determined using a cutoff distance of  $96''$  (5.2 pc for objects at the distance of W49). Right: seven MST subclusters identified with  $N \geq 6$  and  $d_c = 40''$  (2.2 pc). Objects in clusters are colored according to their group, while sources not associated with any clusters are plotted in gray.

**Table 8**  
Properties of the Clusters in W49 GMC for  $d_c = 40''$

No. <sup>a</sup>	Cluster Name	R.A. (J2000.0) ( $^{\circ}$ )	Decl. (J2000.0) ( $^{\circ}$ )	$N_{IR}$ <sup>b</sup>	I	II	II/I <sup>c</sup>	$N_{emb}$ <sup>d</sup>	$N_{td}$ <sup>e</sup>	Diameter ( $''$ )	Diameter (pc)
1a	G43.17-0.00	287.571256	9.102715	9	6	3	0.50(0.35)	0	0	70.53	3.81
1b	G43.10-0.04	287.57085	9.017707	8	3	3	1.00(0.82)	2	0	88.15	4.76
1c	G43.19-0.02	287.597988	9.105411	7	1	6	6.00(6.48)	0	0	34.26	1.85
1d	G43.15+0.03	287.532889	9.096616	7	1	6	6.00(6.48)	0	0	50.86	2.74
1e	G43.13+0.06	287.497549	9.089443	6	1	3	3.00(3.46)	2	0	60.49	3.26
1f	G43.23-0.05	287.639709	9.138874	6	2	4	2.00(1.73)	0	0	38.57	2.08
2a	G43.31-0.08	287.705104	9.185597	6	1	4	4.00(4.47)	1	0	79.40	4.28

<sup>a</sup> Subclusters 1a, 1b, 1c, 1d, 1e, and 1f correspond to cluster 1; subcluster 2a corresponds to cluster 2. Clusters 1, 2, and 3 are determined by the cutoff distance  $d_c = 96''$

<sup>b</sup> Number of stars with infrared excess. Includes Class I, Class II, deeply embedded protostars, and transition disk candidates.

<sup>c</sup> Number in parentheses indicates Poisson uncertainty in ratio.

<sup>d</sup> Number of deeply embedded protostars.

<sup>e</sup> Number of transition disk candidates.

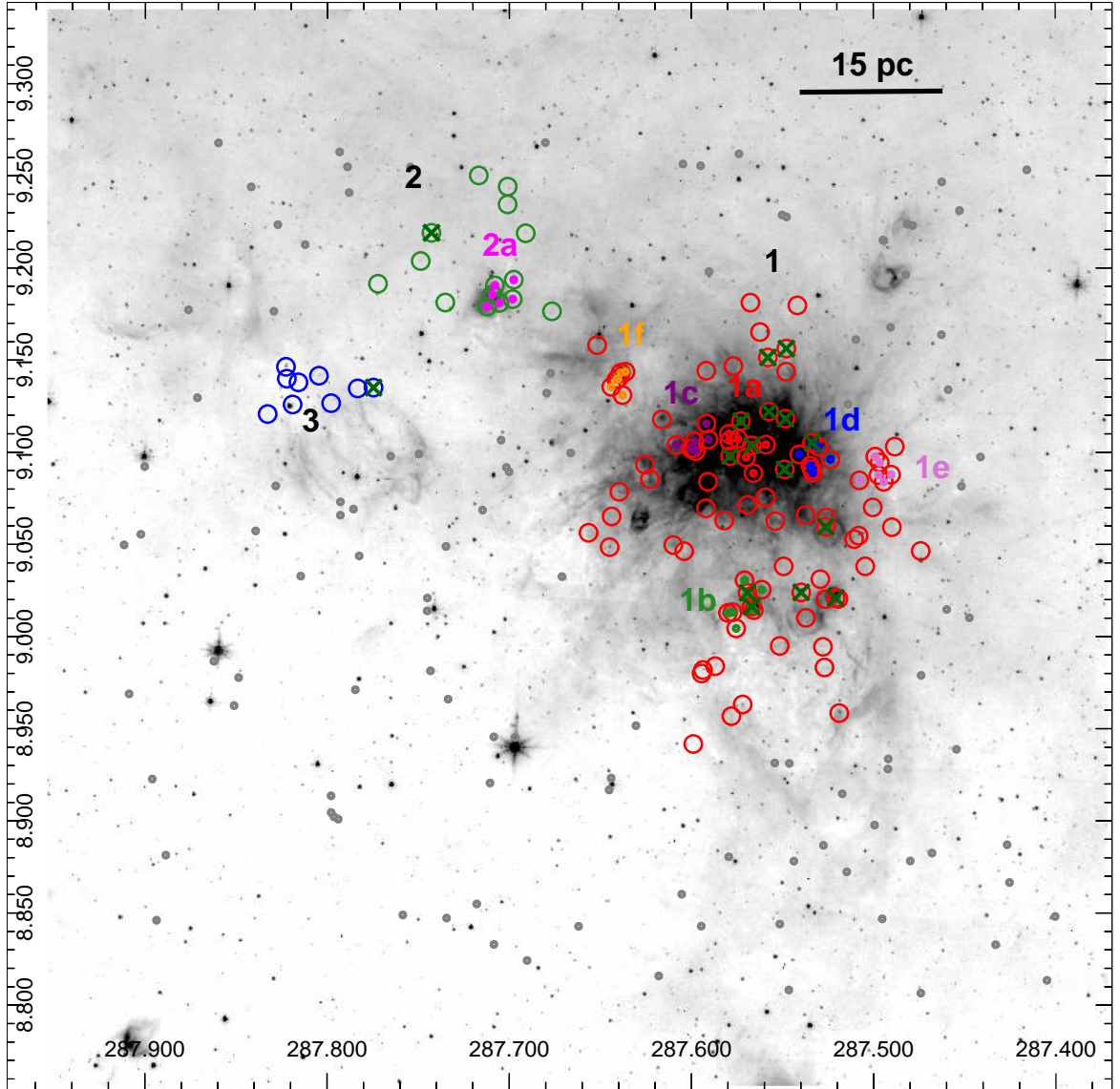


**Figure 12.** Three MST clusters identified using  $d_c = 96''$  are shown with black group numbers overlaid on the IRAC  $8 \mu\text{m}$  image. The seven subgroups identified by  $d_c = 40''$  are shown with a letter and the cluster number they belong to (see Table 7 and Table 8). Massive YSO candidates ( $M > 8 M_{\odot}$ ) are shown with green crosses. Distributed YSO candidates not assigned to groups are plotted with gray points.

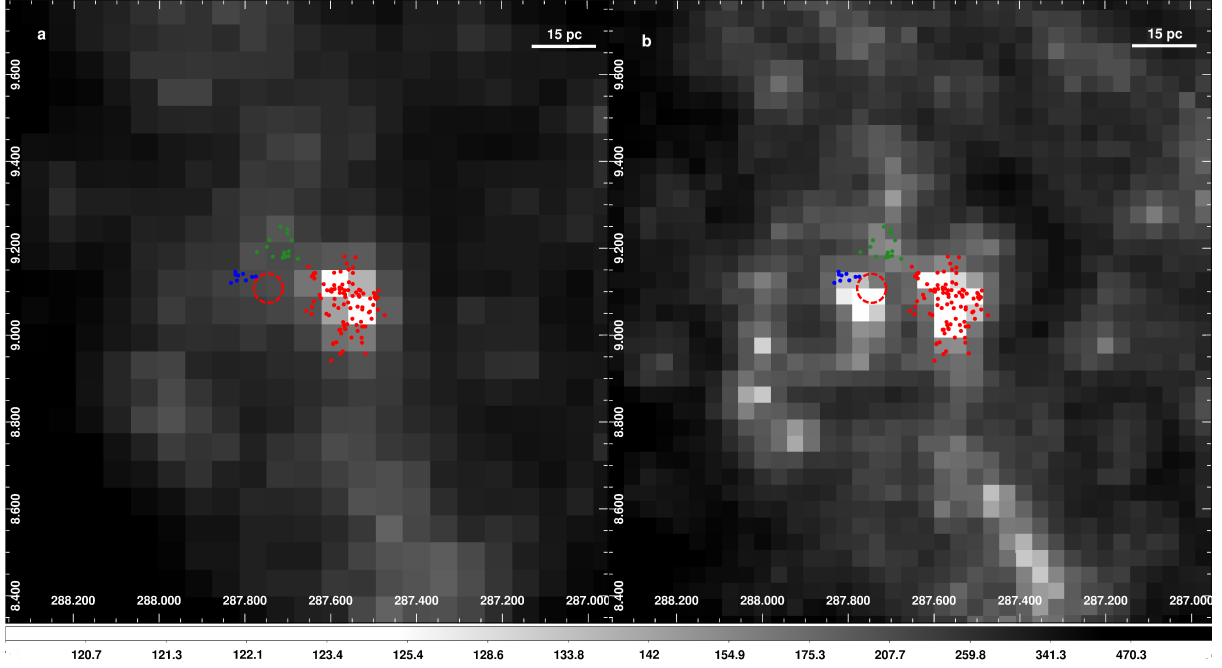


**Figure 13.** YSO nearest-neighbor distance (in arcseconds) in the W49 cloud complex, with the YSO candidates in identified clusters overlayed on each panel. Panel (a) shows the YSO nearest neighbor distance in the W49 cloud complex. Panel (b) shows the YSO nearest neighbor distance including the faint YSOs/possible contaminants. The position of the W49B supernova remnant is indicated by the red circle.

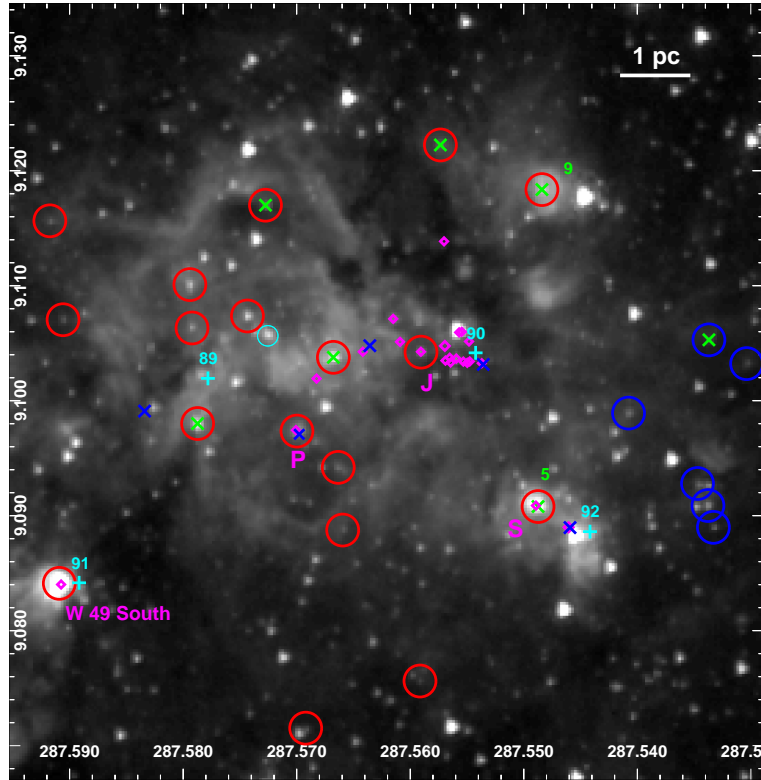


**Figure 14.** Positions of UCHII regions (De Pree et al. 1997) in the W49 field are shown with magenta diamonds on the IRAC 3.6  $\mu\text{m}$  image with the associated YSOs. Red circles show the YSOs in subcluster 1a, and blue circles show the YSOs in subcluster 1d. The cyan circle marks the location of the O type star discovered by Wu et al. (2014). Green crosses mark the massive YSO candidates, cyan crosses 89, 90, 91, and 92 mark the massive dust clumps from Matthews et al. (2009), and blue crosses mark the methanol masers identified by Breen et al. (2015).

This best-fit method is described in detail by Robitaille et al. (2007).

With a limited amount of photometric data, in order to explore all the possible solutions, we first applied the

Azimlu et al. (2015) method, which uses a Markov Chain Monte Carlo method to explore the larger parameter space of the model grid. We applied this method to the set of YSO candidates and found that 78% have masses  $\leq 8 M_{\odot}$ , and 60% of



**Table 9**  
Clusters/Subclusters in W49

Parameter	Straight-line Fit	$d_c=40''$
Number of clusters	3	7
Cutoff distance	96'' (5.2 pc)	40'' (2.2 pc)
Percent in clusters	52	21
Group size/diameter	176''-498'' (9-27 pc)	34''-88'' (1-5 pc)
Class II/I Ratio	2.11(0.43)*	2.00(0.64)*

\* Number in parentheses indicates Poisson uncertainty in ratio.

the YSO candidates have masses between 2 and 6  $M_\odot$ .

Within the set of MYSOs found to be  $\geq 8 M_\odot$ , we selected the ones that have at least six photometric data points to limit the fitting to the better-constrained objects, and we used the Robitaille et al. (2007) online SED fitter to obtain the physical parameters from the best fit. This selection also favors the brighter and possibly more massive objects in our sample. We identified 16 MYSO candidates with this selection method, which are shown in Figure 12 with green crosses.

The SED fitter was used to model the available data (2MASS/UKIDSS  $J$ ,  $H$ , and  $K_s$ , *Spitzer*/IRAC3.6, 4.5, 5.8, and 8.0  $\mu\text{m}$ , and *Spitzer*/MIPS 24  $\mu\text{m}$ ). We focused on only the mass, luminosity, and age parameters; all of the modeled parameters are likely to have a high uncertainty without a finer sampling of the object's SED. To provide some indication of the model accuracy, we report the results from the average of the best 10 fit models and their standard deviation for the YSO candidates that have masses larger than 8  $M_\odot$  in Table 10.

Most of the MYSO candidates are classified as Class I, which shows that they are recently formed. MYSO candidates 1 and 16 were also previously identified as YSOs in the Red MSX Source Survey (RMS; Urquhart et al. 2014). An H II region S at the position of MYSO 5 and another H II region at the position of MYSO 9 were previously identified in the same survey. Within 15'' near MYSO 5 there is another H II region and a methanol maser, which are both indicating that there is ongoing massive star formation (Figure 14).

## 5. MASSIVE STAR FORMATION TRACERS

A large fraction of stars and clusters form mostly at the peripheries of H II regions, and it has been suggested that H II regions can enhance and trigger the massive star formation (e.g., Deharveng et al. 2006, 2008; Zavagno et al. 2006). Since W49 is a massive star-forming complex that hosts many UCHII regions, it is expected to have massive star formation around those locations. As can be seen in Figure 14, most of the H II regions are located within a 1 pc area around the Class I candidate SSTOERC G043.1684+00.0087, where the UCHII region W49 J (De Pree et al. 1997) is located. Four of the H II regions seem positionally associated with YSO candidates, including one MYSO candidate. The close correspondence between some of the YSO candidates and the UCHII regions may indicate that some of the YSOs may be related to the driving object behind these UCHII regions, or at least formed in the same cluster.

Embedded UCHII regions and MYSOs have similar mid-IR colors and very similar ages (Mottram et al. 2011); however, we do not see more associations, contrary to what we expect from these massive star formation tracers. Several of the H II regions are very bright in the IRAC images, and a couple are saturated in the 8.0  $\mu\text{m}$  band. However, most of the H II regions do not have an associated YSO candidate. In some cases

we were not able to classify these sources because of the lack of detection in at least four of our photometric bands. For example, it can be seen in Figure 14 that many of the H II regions close to W49 J do not have bright mid-IR counterparts, and the sources in this region would be difficult to separate at this resolution. It also can be seen that many of the IR-identified candidate MYSOs do not have associated UCHII or dust clump sources, indicating that the sources are perhaps in different evolutionary stages.

In addition to HII regions, methanol masers are also known to be associated with high-mass star-forming regions (Pestalozzi et al. 2002; Breen et al. 2013). The positions of the 6.7 GHz methanol masers identified by Breen et al. (2015) in W49 (G43.149+0.013, G43.165+0.013, G43.167-0.004, G43.171+0.005, and G43.175-0.015) are shown in Figure 14 with blue crosses. These methanol masers appear as unclassified in our catalog according to their lack of photometry; however, G43.167-0.004 seems positionally associated with H II region P and/or one of our Class I YSO candidates which does not appear to be an MYSO candidate according to the SED modeling. Three of the methanol masers seem also positionally associated with previously identified H II regions, as can be seen in Figure 14. These sources are perhaps in a younger stage of evolution where we cannot yet trace them with IR photometry. We can conclude that high-resolution observations in the infrared, submillimeter, and radio are necessary to put together a comprehensive picture of the star formation in the central region of W49.

## 6. DISCUSSION

### 6.1. Star Formation in W49 GMC

Alves & Homeier (2003) found four clusters associated with radio sources W49S, W49N, S, and Q and hypothesized that the GMC collapsed to form the central massive cluster (W49N) and stellar winds and UV radiation triggered the formation of the Welch ring. However, they did not find any evidence of triggering for other clusters on the south and east part of the region (W49S, S, and Q). Also, they indicate that compact H II regions with short lifetimes can be found over the entire region, providing evidence for multiscaled, largely coeval star formation in W49A. In our clustering analysis, we found that the large cluster 1 (G43.15-0.01) represents almost the whole GMC, including the well-known Welch ring, W49S, and clusters S and Q.

There is significant correspondence between our YSO subclusters and the clusters identified by Alves & Homeier (2003). Subcluster 1a (G43.17-0.00) corresponds to their cluster 1 ("Extended"), while their cluster 2, W49A South, is unresolved in the IRAC images and detected as a single YSO candidate (SSTOERC G043.1651-00.0285). Their cluster 3, corresponding to UCHII region S, is also identified as a single high-mass Class I YSO candidate in our data, SSTOERC G043.1518+00.0115. Their cluster 4, corresponding to UCHII region Q, is bright in the IRAC images but did not meet the YSO selection criteria.

The other subclusters we have identified extend to the east and west of W49A and do not correspond to previously identified near-infrared stellar clusters. In total we identified seven subclusters of YSOs within 30 pc of W49A using the MST method. Subclusters 1a, 1b, 1c, 1d, 1e, and 1f correspond to cluster 1 which has a Class II/I ratio of 1.87. Within this cluster, the youngest subcluster 1a, corresponding to the central region of W49A, and subclusters 1c and 1d lie near the out-

**Table 10**  
Physical Parameters of Massive YSO Candidates

No.	Name	R.A. J2000.0(°)	Decl. J2000.0(°)	Mass ( $M_{\odot}$ )	$\sigma$ ( $M_{\odot}$ )	Luminosity ( $10^3 L_{\odot}$ )	$\sigma$ ( $10^3 L_{\odot}$ )	Age ( $10^6$ yr)	$\sigma$ ( $10^6$ yr)	Class
1	SSTOERC G043.0772+00.0038	287.520782	9.021031	12.45	1.29	12.77	3.61	0.84	0.76	1
2	SSTOERC G043.0942-00.0388	287.566986	9.016427	10.15	1.99	3.41	1.08	0.11	0.15	1
3	SSTOERC G043.1017-00.0373	287.569153	9.023827	9.57	0.87	5.51	1.74	2.25	0.70	1
4	SSTOERC G043.1139+00.0169	287.526184	9.059647	7.35	0.50	0.74	0.19	0.08	0.03	2
5	SSTOERC G043.1518+00.0115	287.548737	9.090796	18.96	3.61	34.37	23.66	0.02	0.02	1
6	SSTOERC G043.1578+00.0314	287.533691	9.105292	10.41	2.09	5.38	2.46	0.16	0.15	1
7	SSTOERC G043.1716+00.0017	287.566772	9.103776	8.90	0.63	4.23	0.96	1.30	0.22	1
8	SSTOERC G043.1719-00.0114	287.578735	9.098016	11.13	2.14	9.48	6.26	0.37	0.49	1
9	SSTOERC G043.1761+00.0245	287.548401	9.118363	14.14	3.26	20.10	11.01	0.48	0.31	1
10	SSTOERC G043.1837+00.0185	287.557343	9.122244	12.52	2.23	10.01	3.58	0.16	0.12	1
11	SSTOERC G043.1860+00.0026	287.572754	9.117006	13.37	2.40	16.46	7.27	0.52	0.39	1
12	SSTOERC G043.2096+00.0426	287.547821	9.156357	8.09	0.74	3.27	0.84	2.53	0.94	1
13	SSTOERC G043.2099+00.0315	287.557983	9.151517	14.60	0.00	19.20	0.00	1.30	0.00	2
14	SSTOERC G043.2942-00.1658	287.774597	9.135176	12.03	4.35	13.96	8.54	0.93	0.59	2
15	SSTOERC G043.3542-00.0991	287.742798	9.219168	9.63	0.00	5.50	0.00	3.0	0.00	3
16	SSTOERC G043.0885-00.0114	287.539703	9.024038	17.30	3.45	34.03	16.18	0.17	0.11	1

side edge of the mid-infrared double-ring structure proposed by Peng et al. (2010). The double-ring structure was interpreted as sites of massive star formation triggered by feedback from the central stars in W49A. Because of the large uncertainty in the Class II/I ratios due to small number statistics, the relative ages of subclusters according to the ratio of II/I will not be discussed.

Although clusters 2 and 3 do not have significantly more members than clusters that appear in our random trials, we note that both of these clusters contain MYSO candidate objects, which do not appear outside of our identified clusters. Cluster 2 contains one of the subclusters (2a) that are significant and do not appear outside of the main clusters found at the larger break lengths. It is also associated with a region of enhanced extended IR emission that can be seen in Figure 2. Cluster 3 is adjacent to and may be associated with the supernova remnant W49B. The class II/I ratio of cluster 3 is  $3.50 \pm 2.81$  and may indicate an apparent age intermediate between cluster 1 and cluster 2.

Matthews et al. (2009) identified dust clumps associated with W49 molecular clouds with continuum emission observations at  $850 \mu\text{m}$  with  $15''$  resolution by using *SCUBA/James Clerk Maxwell telescope*. The dust clumps 98 and 100 seem associated with the subcluster 1b (G43.10-0.04) with their given distances between 11.1 and 11.4 kpc determined from  $^{13}\text{CO}(1-0)$  and HI data by Matthews et al. (2009). The rest of the dust clumps, 83, 84, 85, 86, 87, 89, 90, 91, 92, 93, 94, 95, 96, 97, 101, 102, 103, and 104, correspond to the region where we identified cluster 1, and they are shown in Figure 15 with blue crosses. The dust clumps 89, 90, 91, and 92, which are shown in Figure 14, have the biggest masses between  $3.5 \times 10^4$  –  $2.8 \times 10^5 M_{\odot}$ , and it was noted by Matthews et al. (2009) that assuming a dust temperature of 15 K, these massive clumps will eventually form star clusters via fragmentation. Dust clumps shown with orange crosses in Figure 15 were determined to be at distances between 4.03 and 7.45 kpc by Matthews et al. (2009), which might indicate that the clusters 2 and 3 are not associated with the W49 complex. Follow-up observations will be necessary to verify the classification and distance of these YSO candidates and confirm their cluster membership.

## 6.2. Line-of-sight Cloud and W49 MST Clusters

Simon et al. (2001) showed that the GRSMC 43.30-0.33 cloud, which was identified with the Galactic Ring Survey (GRS; Jackson et al. 2006), is near the line of sight to W49 at a distance of 3 kpc and largely overlaps W49. We used the integrated intensity CO maps from Simon et al. (2001) to compare the spatial distributions of YSOs in each cloud. We show the YSO clusters with the CO map contours in Figure 15. Cluster 1 (G43.15-0.01) and the subclusters 1a, 1b, 1c, 1d, 1e, and 1f seem strongly associated with the strongest CO emission in the W49 GMC. Cluster 2 (G43.33-0.08) does not seem strongly associated with the CO emission, and it is roughly in line with a dust clump at a distance of 7.45–7.30 kpc (Matthews et al. 2009). However, it contains an MYSO candidate (SSTOERC G043.3542-00.0991) and subcluster 2a (G43.31-0.08) which seems more strongly associated with the CO emission than the rest of the cluster.

Similarly, on the line of sight of cluster 3 (G43.31-0.20), there is a dust clump at a distance of 4.37–4.10 kpc (Matthews et al. 2009) that might be associated with the foreground cloud GRSMC 43.30-0.33. The Class I YSO candidate closest to the Matthews et al. (2009) dust clump is offset by  $8''$  from a group of infrared sources that are partially resolved into four peaks of emission within a  $4.5''$  aperture in the 3.6 and  $4.5 \mu\text{m}$  images but unresolved at 5.8 and  $8.0 \mu\text{m}$ . However, there is an MYSO candidate in that cluster (SSTOERC G043.2942-00.1658) that could be associated with the CO emission coming from the W49 cloud, as can be seen in Figure 12 and Figure 15. There are no clusters that seem to be associated with the brightest CO emission from GRSMC 43.30-0.33 like we see in W49, and with it being closer to us, we would expect to be able to detect lower-mass and lower-luminosity objects from clusters associated with the foreground cloud. Because of its projected position on the sky, cluster 3 might be thought to have the greatest chance of being a foreground object, potentially associated with GRSMC 43.30-0.33 at 3 kpc, the dust clump at 4.37–4.10 kpc, or the W49B supernova remnant region at more than 10 kpc, as previously mentioned in Section 3.2.2.

## 6.3. Comparison with Other Star-forming Regions

The 11.1 kpc distance to W49 limits our sensitivity to detect only the brightest and most luminous YSO candidates. To better understand W49 in the context of other regions form-

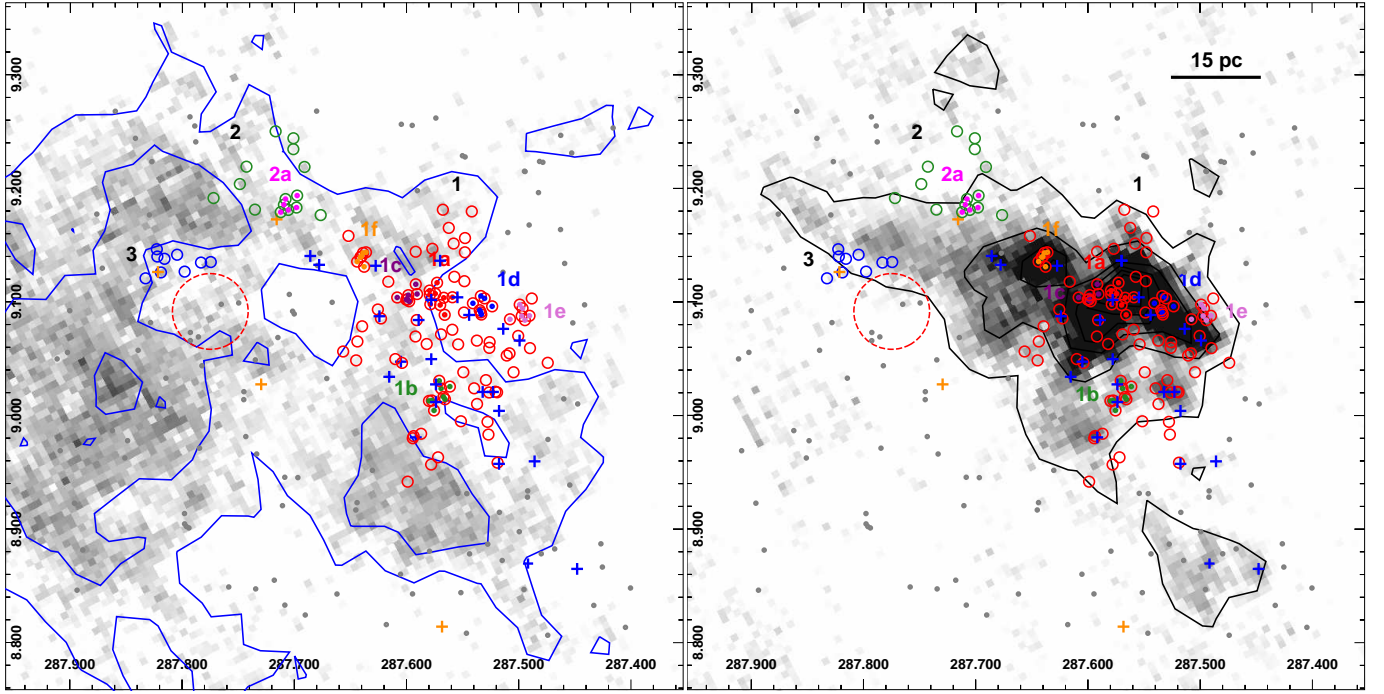


**Figure 15.**  $^{13}\text{CO}(1-0)$  integrated intensity contours (Simon et al. 2001) and YSO clusters overlaid on CO maps in gray scale. Left:  $^{13}\text{CO}(1-0)$  intensity is integrated over the velocity range associated with GRSMC 43.30-0.33 ( $\nu_{\text{LSR}} = 35 - 50 \text{ km s}^{-1}$ ) and contour levels are 2.5, 6.25, 10  $\text{K km s}^{-1}$ , shown in blue; right:  $^{13}\text{CO}(1-0)$  intensity is integrated over the velocity range associated with W49 GMC ( $\nu_{\text{LSR}} = -5 - 25 \text{ km s}^{-1}$ ), and contour levels are 2.5, 14, 25.5, 37, 48.5 and 60  $\text{K km s}^{-1}$  for W49 GMC, shown in black. Blue crosses show the dust clumps determined at 11.1–11.4 kpc, and orange crosses show the dust clumps determined at 4.10–7.30 kpc by Matthews et al. (2009). The red circle indicates the position of the supernova remnant W49B.

ing rich clusters, we investigate how the YSO populations of luminous star-forming complexes G305 and G333 would appear if they were at the greater distance of W49. Taken together, these three regions also probe different evolutionary stages, from deeply embedded sources forming protoclusters to already-revealed open clusters.

G305 ( $l, b = 305^\circ.4, +0^\circ.1$ ; Clark & Porter 2004) is one of the most massive ( $M \gtrsim 6 \times 10^5 M_\odot$ ; Hindson et al. 2010) star-forming complexes in the Galaxy, and is located in the Scutum-Crux arm at an estimated distance of  $\sim 4$  kpc. The complex has a ringlike morphology of bright mid-infrared emission extending over  $\sim 34$  pc that surrounds two optically visible open clusters, Danks 1 and Danks 2. The G305 complex has a considerable amount of ongoing star formation around the periphery of its oldest object, Danks 2 ( $3_{-1}^{+3}$  Myr), and the younger Danks 1 ( $1.5_{-0.5}^{+1.5}$ ) (Davis et al. 2012).

G333 (also known as RCW 106;  $l, b = 333^\circ.3, -0^\circ.4$ ) lies at a distance of 3.6 kpc (García et al. 2014) and extends over 50 pc. It contains a number of H II regions and MYSO candidates, with an estimated bolometric luminosity  $\log(L_{\text{bol}}) = 6.28$ , making it one of the most luminous massive star-forming regions in the Galaxy (Urquhart et al. 2014).

Using the *Spitzer* mid-infrared photometry catalog from Willis et al. (2015), we identified 1189 and 1057 YSO candidates in G305 and G333, respectively, by using the classification method described in Section 2.4, and performed the clustering analysis as described in Section 3.2. We investigate the clustering properties of G305 and G333 both at their assumed distances and as they would appear if projected to the same distance as W49.

These regions have a rich population of YSOs, and we identified 15 YSO clusters with this MST method in the G305 complex using the straight-line fit method determining  $d_c =$

**Table 11**  
Clusters/Subclusters in G305

Parameter	Straight-line Fit	$N_{\text{grp}}$ Max 1
Number of clusters	15	32
Cutoff distance	48'' (0.9 pc)	30'' (0.6 pc)
Percent in clusters	76	44
Group size	36''-911'' (1-18 pc)	9''-295'' (0.2-6 pc)
Class II/I ratio	3.5(0.3)*	3.0(0.3)*

\* Number in parentheses indicates Poisson uncertainty in ratio.

**Table 12**  
Clusters/Subclusters in G333

Parameter	Straight-line Fit	$N_{\text{grp}}$ Max 1
Number of clusters	11	45
Cutoff distance	73'' (1.3 pc)	52'' (0.9 pc)
Percent in clusters	81	54
Group size	110''-1353'' (2-24 pc)	43''-306'' (1-5 pc)
Class II/I ratio	4.5(0.4)*	4.0(0.4)*

\* Number in parentheses indicates Poisson uncertainty in ratio.

48'' and we set  $N \geq 7$  members. With the same method, we found 11 YSO clusters with  $d_c = 73''$  in G333. In order to see the hierarchical structure, we also used a short cutoff distance that maximizes the number of clusters, identifying the clusters shown in Figure 16. The clustering results for these two regions at their original distances are shown in Table 11 and in Table 12.

For a large branch length cutoff, the probability of the ob-



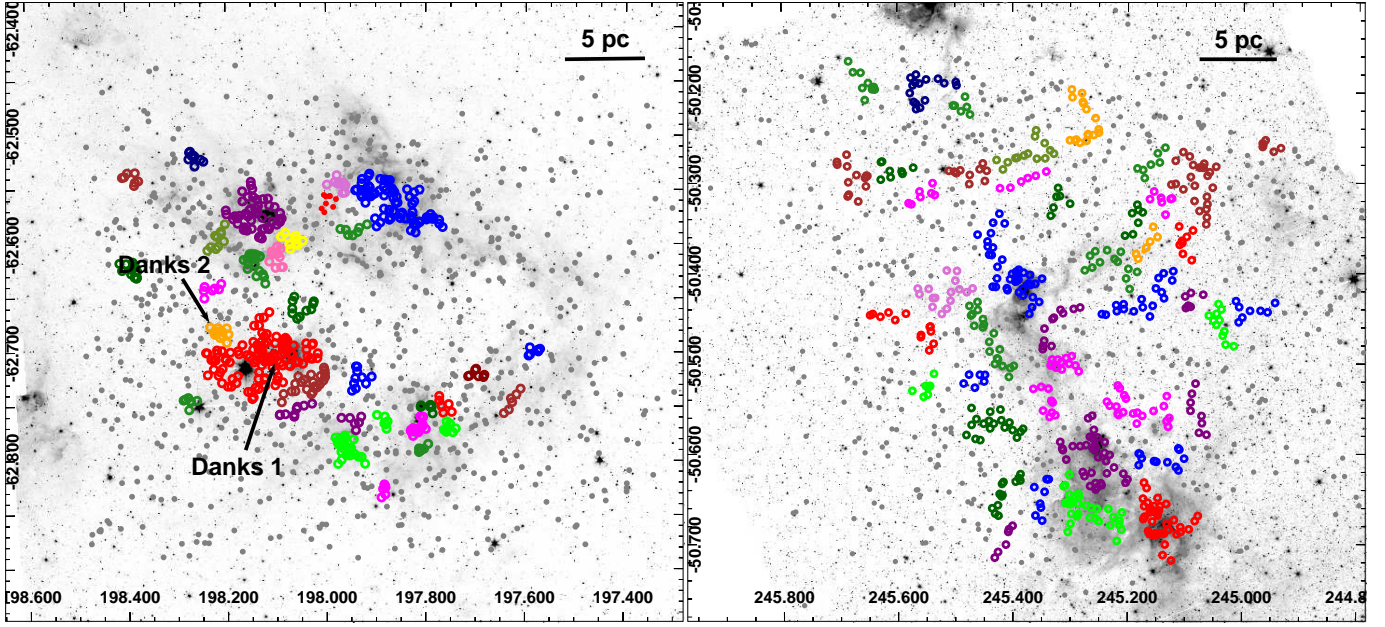


**Figure 16.** Left: subclusters identified in the G305 star-forming region (using  $d_c = 30''$ ) are overlaid on the IRAC 5.8  $\mu\text{m}$  image. Right: subclusters identified in the G333 star-forming region (using  $d_c = 52''$ ) are overlaid on the IRAC 5.8  $\mu\text{m}$  image. Distributed YSO candidates not assigned to groups are plotted with gray points.

served clustering properties occurring randomly is relatively high. In G305 the most significant result is the size of the two largest clusters, which occurred in less than 0.1% of our simulations. In G333 the largest cluster is smaller (378 members) and therefore has a higher probability of occurring randomly (7%).

The results for both clusters are more significant with a shorter cutoff distance. The probability of the G333 subclusters occurring randomly is 3.3%–18.3%, indicating that a larger number of these structures may be randomly connected sets of objects. This is supported by the morphology of the G333 subclusters, which display a significant number of subclusters with very linear or filamentary appearance that occur randomly. The probability of the number and sizes of G305 subclusters occurring randomly is  $< 0.1\%$ , and the clusters also have a strong association with features in the extended IRAC 5.8  $\mu\text{m}$  image, including subclusters associated with both the open clusters Danks 1 and Danks 2.

We determined the projected appearance of the G305 and G333 YSOs by rescaling the relative source positions and magnitudes for a distance shift from 3.6 kpc (G333) and 4 kpc (G305) to the 11.1 kpc distance to W49. We applied a limiting magnitude of 20.3, 19.3, 18.2, 18.6, 16.3, 14.8, 14.3, and 9.4 mag for  $J$ ,  $H$ ,  $K$ , 3.6, 4.5, 5.8, 8.0, and 24  $\mu\text{m}$ , respectively, which are the faintest detections in the W49 field with error smaller than 0.2 mag. After reprojecting the source coordinates, we did not find any overlapping sources within the same photometric aperture ( $2''$ ) at the rescaled distance.

After rescaling, we reclassified all the sources as described in Section 2.4. We do not assume any additional reddening, so the colors of the objects do not change after projecting. However, sources may be below the applied limiting magnitude from the W49 catalog in one band and above in others, resulting in a change in the source classification based on the new, more limited wavelength coverage.

The new projected catalog for G305 contains 696 YSOs, only 59% of YSOs from the original catalog, and the projected catalog for G333 contains 404 YSOs, only 38% of the

original YSOs. In Section 2.4 we applied a cut for sources with  $[3.6] > 13$  to remove likely background objects from the YSO sample. When we apply the same cut to the projected G305 YSOs, the resulting population is 6.9% of the original size, and for G333 the resulting YSO population after applying the faint-object cut is 7.9%.

The field of view for G305 and G333 was approximately the same at their original distances,  $0.5^\circ \times 0.5^\circ$ . After reprojecting G305, the area decreases to  $0.18^\circ \times 0.18^\circ$  and the G333 area decreases to  $0.16^\circ \times 0.16^\circ$ . We applied the MST clustering analysis to the G333 and G305 YSO populations at both their original and projected distances, comparing to simulated random clusters for each set of YSO population and observed or projected area parameters.

In Section 3.2.1, the straight-line fit method for W49 appeared to identify GMC-scale clusters. For the rescaled clusters without cutting off sources that fall below the  $[3.6] = 13$  mag cut, we used only the straight-line fit method. For the rescaled G305 we derived the cutoff distance as  $22''$  (corresponds to  $d_c = 1.2$  pc, at a distance of 11.1 kpc) and for the rescaled G333 we derived the cutoff distance as  $33''$  (corresponds to  $d_c = 1.8$  pc, at a distance of 11.1 kpc). For G305 and G333 the reprojected straight-line fit cutoff distance finds only one cluster per region, with a clustered fraction of 74% in rescaled G305 and 81% in G333.

Finally, we examined the clusters in the rescaled G305 and G333 as they would appear if we removed the sources fainter than  $[3.6] = 13$ . The straight line-fit cutoff distance without faint sources was  $52''$  for G305 and  $78''$  for G333. Although these are shorter cutoff distances than W49, the clusters found are not highly significant. The largest cluster in rescaled G333 has only 51 members, only half the size of cluster 1 in W49. The chance of the largest rescaled G333 cluster occurring randomly was 3.2%, compared to  $< 0.1\%$  for cluster 1 in W49. The G305 rescaled clusters were smaller, but because of their shorter cutoff distance, they were also more significant. The largest cluster in rescaled G305 had only 32 members, a size that was met in only 0.2% of our simulated rescaled G305

clusters.

To directly compare the sizes and numbers of the clusters in W49 to G305 and G333, we also determined the clustering properties in G305 and G333 using the W49 parameters from the straight-line fit ( $d_c = 96''$  with  $N > 7$ ) and the peak that maximized the number of groups ( $d_c = 40''$  with  $N > 6$ ). We found only one cluster with  $d_c = 96''$ , and although the clusters are larger than for the best-fit cutoff distance for G305 and G333 individually, they are still smaller than the largest cluster in W49. This indicates that W49 has a larger population of high-luminosity YSOs than either G333 or G305. With  $d_c = 40''$  we found three clusters in G333 and five clusters in G305, with similar size distributions to W49 clusters 1a–1f and 2a, as can be seen in Figure 17. There were three clusters in only 0.3% of the rescaled G333 simulations, and there were five clusters in only 0.2% of the rescaled G305 simulations. The number and size distributions of the subclusters in G305, G333, and W49 are all significant, although W49 again has the richest population, with seven subclusters found. In W49, six of the seven clusters are found within an area of approximately  $0.15^\circ \times 0.15^\circ$ , comparable to the projected area of G305 and G333 and indicating that the larger number of tightly packed clusters in W49 is not simply due to the larger field. The W49, G305, and G333 clustering properties and associated probabilities are all summarized in Table 13.

#### 6.4. Class II/I Ratio as a Cluster Age Indicator

As seen in Table 14, the Class II/I ratios in G305 and G333 change when the YSOs are reprojected to W49 distance, and because of its higher Class II/I ratio, W49 appears oldest and the G305 region appears to be the youngest. However, as we mentioned in Section 6.3, G305 has an older population with its two open clusters. This drop in Class II/I ratio in G305 and G333 regions after rescaling to the greater distance is mainly because lower-luminosity Class II YSOs drop below our detection limits before Class I YSOs do, biasing our observations of distant regions toward younger objects. This effect must be taken into account when comparing clouds at different distances using the Class II/I ratio as an age indicator.

### 7. SUMMARY

In this paper, we combined *Spitzer* IRAC (3–8  $\mu\text{m}$ ), MIPS (24  $\mu\text{m}$ ), and UKIDSS near-IR ( $JHK_S$ ) data for the W49 GMC to identify and classify YSOs by using their infrared colors and magnitudes and analyzed their clustering properties according to their spatial distribution across the region. We found the following numbers of YSO candidates: 186 Class I, 907 Class II, 74 transition disks, and 46 deeply embedded protostellar sources. We used the MST method to identify the groups and subclusters in the region and found that 52% of YSOs (including transition disk objects) belong to clusters of  $\geq 7$  members in the W49 GMC. In order to assess the significance of the identified MST clusters, we performed simulations on randomly distributed YSOs and examined the probability of finding random clusters. We found that cluster 1 represents a large-scale structure in the cloud extending  $\sim 27$  pc in diameter, with a very low probability of occurring in a random distribution of sources. This cluster is centered on the previously identified main W49 region with many tracers of high-mass star formation detected. We also used a smaller cutoff distance to investigate the hierarchical structure in the cloud, finding several subclusters within the larger clusters. The distribution of identified subclusters has a very low probability of occurring randomly.

We applied an SED fitting method to 231 YSO candidates in the MST clusters in order to identify the most massive candidates in our sample and found 16 YSO candidates that have masses  $\geq 8 M_\odot$ . We found that the massive Class I candidate SSTSERC G043.1518+00.0115 is located at the position of the UCHII region W49 S. However, we could not find any more associations because most of the H II regions are unclassified in our catalog owing to lack of photometry. We also examined previously identified methanol masers in the region that are known as good indicators of high-mass star formation. However, we do not find any IR-identified MYSO candidates that appear physically associated with those masers.

We compared the W49 region to two other star-forming regions, G305 and G333. In our cluster analysis we used the cutoff distances and the ratio of class II/I sources in each cloud in order to derive information about their relative ages and YSO densities. In order to directly compare them, we determined the projected appearance of the G305 and G333 regions and compared the number and size distributions of the subclusters. We saw that there are more clusters in the W49 region, which indicates that W49 has the richest population of high-luminosity YSOs. However, we could not use the ratio of Class II/I objects as an age indicator of clusters, since at greater distances we lose a significant number of older objects, which biases our observations. This comparison also indicates that there is potentially a large number of YSOs in W49 that we have not detected.

This work is based in part on observations made with the *Spitzer Space Telescope*, which is operated by the Jet Propulsion Laboratory, California Institute of Technology, under a contract with NASA. Support for this work was provided by NASA. This publication makes use of data products from the Two Micron All Sky Survey, which is a joint project of the University of Massachusetts and the Infrared Processing and Analysis Center/California Institute of Technology, funded by the National Aeronautics and Space Administration and the National Science Foundation. The authors gratefully acknowledge the referee for useful comments and additional discussion. G. S. acknowledges partial support from NASA Grant NNX12AI60G and Istanbul University grant BAP50195 since this work is part of her PhD thesis research.

*Facilities:* 2MASS ( $JHK_S$ ), *Spitzer* (IRAC, MIPS), UKIRT ( $JHK_S$ )

### REFERENCES

- Allen, L., Calvet, N., D'Alessio, P., et al. 2004, *ApJS*, 154, 363
- Alves, J., Homeier, N. 2003, *ApJ*, 589, 45
- Azimlu, M., Martinez-Galarza, J. R., and Muench, A. A. 2015, *ApJ*, 150, 95
- Bastian, N., Ercolano, B., Gieles, M., et al. 2007, *MNRAS*, 379, 1302
- Beerer, I. M., Koenig, X. P., Hora, J. L., et al. 2010, *ApJ*, 720, 679
- Billot, N., Schisano, E., Pestalozzi, M., et al. 2011, *ApJ*, 735, 28
- Breen, S. L., Fuller, G. A., Caswell, J. L., et al. 2015, *MNRAS*, 450, 4109
- Breen, S. L., Ellingsen, S. P., Contreras, Y., et al. 2013, *MNRAS*, 435, 524
- Bressert, E., Bastian, N., Gutermuth, R., et al. 2010, *MNRAS*, 409, 54
- Buckley, H. D., and Ward-Thompson, D. 1996, *MNRAS*, 281, 294
- Cartwright, A., and Whitworth, A. P. 2004, *MNRAS*, 348, 589
- Casali, M., Adamson, A., Alves de Oliveira, C., et al. 2007, *A&A*, 467, 777
- Chavarría, L., Allen, L., Brunt, C., et al. 2014, *MNRAS*, 439, 3719
- Clark, J. S., and Porter, J. M. 2004, *A&A*, 427, 839
- Cutri, R. M. et al. 2013, *yCat*, 2328, 0
- Davies, B., Clark, J. S., Trombly, C., et al. 2012, *MNRAS*, 419, 1871
- De Pree, C. G., Mehringer, D. M. and Goss, W. M. 1997, *ApJ*, 482, 307
- De Pree, C. G., Wilner, D. J., Goss, W. M., et al. 2000, *ApJ*, 540, 308
- Deharveng, L., Lefloch, B., Massi, F., et al. 2006, *A&A*, 458, 191

**Table 13**  
W49, G305, and G333 Clustering Comparison

Region <sup>a</sup>	Cutoff Distance	First Cluster Size <sup>b</sup>	Second Cluster Size	Third Cluster Size	Groups $> N_{min}$ <sup>c</sup>
W49	96''	97	15	9	3
Straight-Line Fit		$< 0.1\%$	66.6%	99.3%	99.9%
W49	40''	9	8	7	7
Peak		0.2%	$< 0.1\%$	$< 0.1\%$	$< 0.1\%$
G333	73''	378	309	39	11
Straight-line fit		7%	$< 0.1\%$	99%	99.9%
G333	52''	40	39	37	45
Peak		3.3%	$< 0.1\%$	$< 0.1\%$	$< 0.1\%$
G305	48''	418	328	26	15
Straight-line fit		$< 0.1\%$	$< 0.1\%$	99.9%	99.9%
G305	30''	113	78	49	32
Peak		$< 0.1\%$	$< 0.1\%$	$< 0.1\%$	$< 0.1\%$
G333 rescaled	78''	51	6	...	2
Straight-line fit		3.2%	99%	...	99.9%
G333 rescaled	52''	24	18	...	2
Peak		$< 0.1\%$	$< 0.1\%$	...	65%
G305 rescaled	52''	32	10	10	4
Straight-line fit		0.2%	29.3%	4.9%	19.3%
G305 rescaled	40''	19	10	10	5
Peak		0.1%	0.2%	$< 0.1\%$	0.2%
G333 rescaled	96''	57	...	...	1
W49 straight-line dist.		55.8%	...	...	99.9%
G333 rescaled	40''	13	8	7	3
W49 peak dist.		0.2%	$< 0.1\%$	0.1%	0.3%
G305 rescaled	96''	74	...	...	1
W49 straight-line dist.		85%	...	...	99.9%
G305 rescaled	40''	19	10	10	5
W49 peak dist.		0.1%	0.2%	$< 0.1\%$	0.2%

<sup>a</sup> Rescaled G305 and G333 do not contain sources below the  $[3.6] = 13$  cut

<sup>b</sup> Percentage is showing the probability of the clusters to occur randomly.

<sup>c</sup>  $N_{min}=6$  for peak and  $N_{min}=7$  for straight-line fit

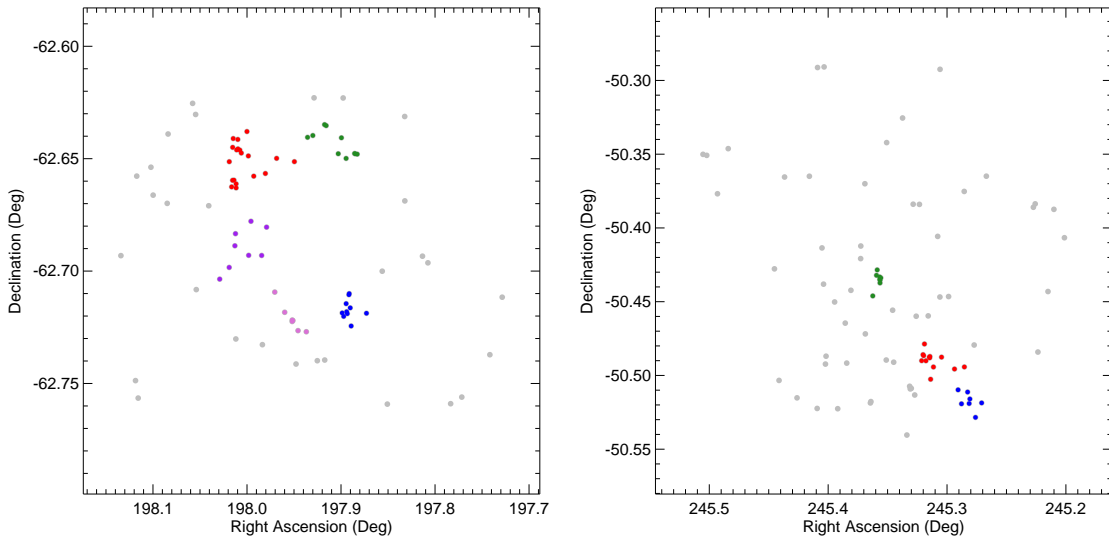


**Figure 17.** Left: subclusters identified in the rescaled G305 star-forming region using the W49 cutoff distance  $d_c = 40''$ . The YSOs are plotted in colors according to the clusters identified. The distributed YSO candidates not assigned to groups are plotted with gray points. Right: same as the left panel, but for G333.



**Table 14**  
Clustering Analysis Summary

Region <sup>a</sup>	Cutoff Distance('')	Cutoff Distance (pc)	Class II/I Ratio <sup>b</sup>
W49	96	5.2	1.8(0.4)
G305	48	0.9	3.5(0.3)
Rescaled G305	96	5.2	0.5(0.1)
G333	73	1.3	4.5(0.4)
Rescaled G333	96	5.2	1.0(0.3)

<sup>a</sup> W49 parameters from straight-line fit  $d_c = 96''$  have been used here to directly compare the biggest clusters in the rescaled regions without sources fainter than  $[3.6] = 13$

<sup>b</sup> Number in parentheses indicates Poisson uncertainty in ratio.

Deharveng, L., Lefloch, B., Kurtz, S., et al. 2008, A&A, 482, 585  
 Dickel, Helene R. and Goss, W. M. 1990, ApJ, 351, 189  
 Dreger, J. W., Johnston, K. J., Welch, W. J., et al., 1984, ApJ, 283, 632  
 Fazio G. G., Hora, J. L., Allen, L. E., et al. 2004, ApJS, 154, 10  
 Gálvan-Madrid, R., Liu, H. B., Zhang, Z.-Y., et al. 2013, ApJ, 779, 121  
 García, P., Bronfman, L., Nyman, L.-Å., et al. 2014, ApJS, 212, 2  
 Guarcello, M. G., Drake, J. J., Wright, N. J., et al. 2013, ApJ, 773, 135  
 Gutermuth, R. A., Myers, P. C., Megeath, S. T., et al. 2008, ApJ, 674, 336  
 Gutermuth, R., Megeath, S. T., Myers, P. C., et al. 2009, ApJS, 184, 18  
 Gutermuth, R., and Heyer, M. 2015, AJ, 149, 64  
 Gwinn, C. R., Moran, J. M., and Reid, M. J. 1992, ApJ, 393, 149  
 Hindson, L., Thompson, M. A., Urquhart, J. S., et al. 2010, MNRAS, 408, 1438  
 Homeier, N. L., Alves, J. 2005, A&A, 430, 481  
 Hora, J., Fazio, G. G., Allen, L. E., et al. 2004, in Mather J., ed., Proc. of the SPIE: Optical, Infrared, and Millimeter Space Telescopes, Vol. 5487, p. 77  
 Jackson, J. M., Rathborne, J. M., Shah, R. Y., et al. 2006, ApJS, 163, 145  
 Koenig, X. P., Allen, L. E., Gutermuth, R. A., et al. 2008, ApJ, 688, 1142  
 Koenig, X. P., Leisawitz, D. T. 2014, ApJ, 791, 131  
 Kuhn, Michael A., Povich, M. S., Luhman, K. L., et al. 2013, ApJS, 209, 29  
 Lada C. J., 1987, in Peimbert M., Jugaku J., eds, Proc. IAU Symp., Vol. 115, Star Forming Regions. Reidel, Dordrecht, p. 1  
 Lada, C. J., Adams, F. C. 1992, ApJ, 393, 278  
 Lada, C. J., Lada, E. A. 2003, ARA&A, 41, 57

Lawrence, A., Warren, S. J., Almaini, O., et al. 2007, MNRAS, 379, 1599  
 Lucas, P. W., Hoare, M. G., Longmore, A., et al. 2008, MNRAS, 391, 136  
 Makovoz, D. & Khan, I. 2005, Astronomical Data Analysis Software and Systems XIV, 347, 81  
 Matthews, H., Kirk, H., Johnstone, D., et al. 2009, ApJ, 138, 1380  
 Mezger, P. G., Schraml, J., and Terzian, Y. 1967, ApJ, 150, 807  
 Mottram, J. C., Hoare, M. G., Davies, B., et al. 2011, ApJ, 730, L33  
 Peng, T.-C., Wyrowski, F., van der Tak, F. F. S., et al. 2010, A&A, 520, AA84  
 Pestalozzi, M., Humphreys, E. M. L., and Booth, R. S. 2002, A&A, 384, L15  
 Pipher, J. L., McMurtry, C. W., Forrest, W. J., et al. 2004, Proc. SPIE, 5487, 234  
 Robitaille, T. P., Whitney, B. A., Indebetouw, R., Wood, K., and Denzmore, P. 2006, ApJS, 167, 256  
 Robitaille, T. P., Whitney, B. A., Indebetouw, R., and Wood, K. 2007, ApJS, 169, 328  
 Robitaille, T. P., Meade, M. R., Babler, B. L., et al. 2008, AJ 136, 2413  
 Schuster, M. T., Marengo, M., and Patten, B. M. 2006, Proc. SPIE, 6270, 20  
 Serabyn, E., Guesten, R., and Schulz, A. 1993, ApJ, 413, 571  
 Sievers, A. W., Mezger, P. G., Bordeon, M. A., et al. 1991, A&A, 251, 231  
 Simon, R., Jackson, J. M., Clemens, D. P., et al. 2001, ApJ, 551, 747  
 Skrutskie, M. F., Cutri, R. M., Stiening, R., et al. 2006, AJ, 131, 1163.  
 Stern, D., Eisenhardt, P., Gorjian, V., et al. 2005, ApJ, 631, 163  
 Stetson, P. B. 1987, PASP, 99, 191  
 Taylor, M. B. 2005, Astronomical Data Analysis Software and Systems XIV, 347, 29  
 Torres, R. M., Loinard, L., Mioduszewski, A. J., and Rodríguez, L. F. 2009, ApJ, 698, 242  
 Urquhart, J. S., Figura, C. C., Moore, T. J. T., et al. 2014, MNRAS, 437, 1791  
 Welch, W. J., Dreher, J. W., Jackson, J. M., et al. 1987, Science, 238, 1550  
 Werner, M. W., Roellig, T. L., Low, F. J., et al. 2004, ApJS, 154, 1  
 Westerhout, G. 1958, Bull. Astron. Inst. Netherlands, 14, 215  
 Willis, S., Marengo, M., Allen, L., et al. 2013, ApJ, 778, 96  
 Willis, S., Guzman, A., Marengo, M., et al. 2015, ApJ, 809, 87  
 Wilner, D. J., De Pree, C. G., Welch, W. J., and Goss, W. M. 2001, ApJ, 550, 81  
 Wu, S.-W., Bik, A., Henning, T., et al. 2014, A&A, 568, LL13  
 Zavagno, A., Deharveng, L., Comerón, F., et al. 2006, A&A, 446, 171  
 Zhang, B., Reid, M. J., Menten, K. M., et al. 2013, ApJ, 775, 79